Exploring the thermal behaviour of the solvated structures of Nifedipine

Authors

Eleanor C. L. Jones[a]*, Kate E. Goldsmith[a], Martin R. Ward[a], Luis M. Bimbo[abc] and Iain D.H. Oswald[a]*

[a]Strathclyde Institute of Pharmacy and Biomedical Sciences, University of Strathclyde, 161 Cathedral Street, Glasgow, G4 0RE, United Kingdom

[b] Department of Pharmaceutical Technology, Faculty of Pharmacy of the University of Coimbra, University of Coimbra, Coimbra, Portugal

[c]Centre for Neuroscience and Cell Biology (CNC) and Centre for Innovative Biomedicine and Biotechnology (CIBB), University of Coimbra, Coimbra, Portugal

Correspondence email: eleanor.jones@strath.ac.uk; iain.oswald@strath.ac.uk

Synopsis   We have explored the solvate formation of nifedipine and probed the desolvation pathways through a combination of Variable-Temperature X-ray powder diffraction and thermal methods.

Abstract   Understanding the solvation of pharmaceutical materials is an important part of materials discovery and development. The isolation and desolvation pathways can provide routes to new polymorphs as well as providing important information of intermolecular interactions that can be formed. Providing detailed *in-situ* structural data is vital to be able to fully characterise changes that may occur in the system. In this paper, we describe the isolation and characterisation of seven solvates of the L-type calcium channel antagonist, nifedipine using variable temperature powder X-ray diffraction so that the structural evolution as a function of temperature can be followed. The solvates reported herein can be split into those that are structurally similar to the previously reported DMSO and Dioxane solvates and those that have a unique crystal structure. Of particular note is the solvate with THF which has a hydrogen-bonding motif between the nifedipine molecules very similar to the metastable β-nifedipine. In addition to variable-temperature X-ray diffraction, the stability of the solid-forms was assessed using differential scanning calorimetry and thermogravimetric analysis and indicate that in all cases desolvation results in the thermodynamically stable α-polymorph of nifedipine even the THF solvate. From the diffraction data the pathway of desolvation during heating of the DMF solvate showed conversion to another likely 1:1 polymorph before desolvation to α-nifedipine. The desolvation of this material indicated a two-stage process; first the initial loss of 90% of the solvent before the last 10% on melting. The methanol solvate shows interesting negative-thermal expansion on heating, which

1

is rarely reported in organic materials, but this behaviour can be linked back to the winerack-type hydrogen bonding pattern of the nifedipine molecules.

Keywords: solvate; desolvation; nifedipine; pharmaceutical; variable-temperature X-ray diffraction.

1. Introduction

The screening process of pharmaceutical materials is an important step in understanding their solid forms landscape. As part of this, recrystallization of an API from different solvents is commonly performed which often results in the isolation of a solvated solid form of the API. This is typically not desirable as solvates are prone to desolvate/convert form during storage and secondary processing that can result in deterioration of the intended pharmaceutical formulation. For example, levothyroxine is commercially used in its pentahydrate form (LSP), to treat hypothyroidism. However, LSP is susceptible to dehydration to the monohydrate form when stored under elevated temperature and low relative humidity; such instability is undesirable.(Shah *et al.*, 2019) This product has been known to be recalled due to issues with chemical and physical stability, however since there is no alternative treatment available, the instability needs to be addressed.(Kaur & Suryanarayanan, 2021) Therefore, there is a requirement to study and understand the formation and collapse of solvated materials alongside their properties so that the risks of their use can be mitigated against.

There have been a number of pharmaceutical solvates that have been thoroughly investigated, including Sorafenib tosylate, ciclesonide, olanzapine, gallic acid and trimesic acid, and even solvated co-crystals.(Yang *et al.*, 2019; Zhou *et al.*, 2016; Bhardwaj *et al.*, 2013; Braun *et al.*, 2013; Ward & Oswald, 2020; Bodart *et al.*, 2021; Liu *et al.*, 2019; Marjo *et al.*, 2011; Moreno-Calvo *et al.*, 2011; Nowak *et al.*, 2022) The stability of solvates is a major consideration such that in some cases it is problematic but in others can be used to improve the physical properties of the material, similar to cocrystallization. For example, the ethanol solvate of Pranlukast (a drug used in the treatment of asthma) has been shown to be four times more soluble than the stable hemi-hydrate form. However, the ethanol solvate transforms to the hemi-hydrate at 90% relative humidity which limits the ability for the more soluble solvate to be taken forward in development.(Furuta *et al.*, 2015) There have been a number of desolvation studies that have tried to resolve and understand solvate formation and the structural relationships between the solvate and the polymorphs of the desolvated product.(Aitipamula *et al.*, 2011; Minkov *et al.*, 2014; Yang *et al.*, 2019) Olanzapine solvates have been extensively studied by Bhardwaj and co-authors.(Bhardwaj *et al.*, 2013) In their study, a relationship between the packing of 18 isomorphous solvates and the pure thermodynamically stable Form I was established which helped to rationalise its formation during desolvation.(Bhardwaj *et al.*, 2013) In addition, Crystal Lattice Energy calculations indicated that olanzapine is not able to form dense packing arrangements, but the common layered structure enables it to be a prolific solvate former. A further study of aripiprazole showed that the hydrogen-bonding pattern of the API in the solvate crystal

2

structure can be retained on desolvation to produce a specific polymorph. Using the structures from three solvate (methanol, ethanol & dichloromethane), Form III was reproducibly isolated due to the dimer hydrogen bonding motif common to all structures.(Braun *et al.*, 2009) But despite these instances of projecting the outcome of a desolvation based on the packing of the solvate and the pure forms, it is not always possible to do so. (Aitipamula *et al.*, 2011) It is clear that in order to gain a better understanding of desolvation processes and be able to use this routinely to access new forms, *in-situ* structural measurements are required to follow the pathway of structural changes that occur.

In this paper, we aim to assess the potential relationship between solvated crystal structure and resulting desolvated forms using a known pharmaceutical compound, nifedipine (3,5-dimethyl 2,6-dimethyl-4-(2-nitrophenyl)-1,4-dihydropyridine-3,5-dicarboxylate, NIF, Scheme 1). We investigated the solvation of NIF in a range of 18 solvents and subsequent desolvation as a method to access metastable forms. The metastable polymorphs (β to δ; Table 1) of NIF have only been isolated from the melt which indicates that these forms are sufficiently stable for identification under ambient conditions. In this study, we have been able to identify novel solvates and track their desolvation through Variable-Temperature X-ray diffraction (single-crystal and powder; VT-XRPD) enabling the structural characterisation as a function of heating. The structural work is supplemented with Thermogravimetric-Differential Scanning Calorimetry (TGA/DSC) to support the crystallographic observations.
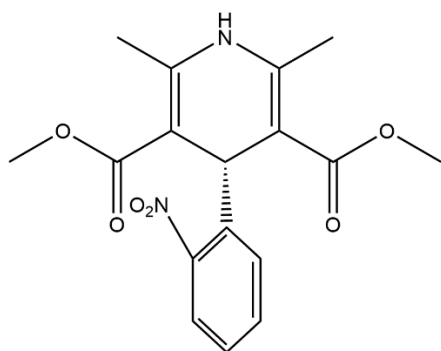
Scheme 1: The molecular diagram of nifedipine.

2. Experimental

2.1. Materials

An excess of NIF (Alfa Aesar, purity 98%) was suspended and slurried in selected solvents (1g/mL) for 24 hours using a magnetic stirrer to agitate the slurry (*ca.* 295 K). A list of solvents used in this study can be found in Table S2 in the ESI. Solid material was separated from the solution using a centrifuge and dried between filter paper before analysis. The supernatant solution was filtered using a 0.2 µm PTFE filter into clean glass vials and covered with pierced lids to aid slow evaporation of the solvent and obtain single crystals for analysis. NIF decomposes when exposed to light, therefore vials

3

were wrapped in aluminium foil to minimise exposure to light and stored in a fumehood until suitable crystals were obtained.

2.2. Single-crystal diffraction

X-ray diffraction data of α-NIF, recrystallised from ethanol, were collected using a Bruker D8 Venture diffractometer with IμS Microfocus Source (Cu Kα1 – 1.54178 Å) and Photon II detector at 297 K. Data were reduced using Apex 3 software, incorporating SAINT V8.40B. SADABS was used for absorption correction.(Sheldrick, 1996) Samples were cooled using an Oxford Cryosystems Cryostream 800 system.(Cosier & Glazer, 1986) The following solvated structures were collected at 100 K, with the exception of DMA, which was collected at 173 K (due to a phase transition below this temperature): pyridine, morpholine, tetrahydrofuran, dimethylacetamide, dimethylformamide, dimethyl sulfoxide, methanol. Further diffraction data were collected on the methanol solvate on a Bruker Kappa APEX II with IμS Microfocus Source (Mo Kα1 – 0.71073Å) and APEX II CCD detector. Data were reduced using similar procedures as above. For the low temperature behaviour of the methanol solvate, variable temperature data of a single crystal of the methanol solvate were collected in 25 K increments from 100 to 275 K using an Oxford Cryosystems Cryostream 800 system.(Cosier & Glazer, 1986) Diffraction data for the 1,4-dioxane solvate was collected using a Synergy-I with Hybrid Pixel Array detector, at 100 K. Data were reduced using CrysAlisPro with SCALE 3 ABSPACK correction implemented.(Rigaku Oxford Diffraction, 2021)

All structures were solved using ShelXT (Sheldrick, 2015*b*) intrinsic phasing incorporated in the Olex2 software (Dolomanov *et al.*, 2009). Refinements were carried out using ShelXL (Sheldrick, 2015*a*) least-squares refinement. Non-hydrogen atoms were anisotropically refined before the addition of hydrogen atoms. Three structures showed disorder in the solvate molecules: tetrahydrofuran, morpholine and dimethylacetamide. To model these, the occupancy of morpholine and tetrahydrofuran atoms were set at 0.5 through the use of the 'Split' function in Olex2. The atoms in the second component were moved to positions where residual electron density was highest. The atoms were being modelled around an inversion centre and so we decided to model the whole molecule at 0.5 occupancy rather than half the molecules at occupancy of 1; this also helped us to create the z-matrix for refinement against our powder diffraction data. The atoms in the dimethylacetamide molecule were split using the same procedure, with atoms refined before fixing the occupancy to 0.85 in molecule one and the remaining molecules occupancy set to 0.15. Distances between atoms were restrained with the SADI atoms, DFIX restraint, and EADP constraints applied. All crystallographic data is located in the supporting information (Table S3 in ESI).

4

2.3. X-ray Powder diffraction

Screening of the X-ray powder diffraction patterns of the samples was carried out using a Bruker D8 Advance II powder diffractometer with a multi-well flat plate, Cu X-ray source (Ka1 = 1.5406 Å) at 297 K. An angular range of 4-35° 2θ with 0.017° 2θ step size with 1 second exposure per step was used. Excess solvent was removed from samples using filter paper prior to placing on a 28-well plate constructed from steel with Kapton film backing. From this data, samples of interest were identified and subject to further data collection in capillary transmission geometry as described below.

2.4. Variable-temperature X-ray powder diffraction

Solids from the slurry experiments were lightly ground to break up any aggregates using an agate pestle and mortar and transferred to 0.7 mm diameter borosilicate glass capillaries. A Bruker D8 Advance diffractometer with Johansson monochromator (Cu Kα1 – 1.5406 λ) was used to collect the data. Samples were heated in 5 K increments (360 K/min) using an Oxford Cryosystems Cryostream 800 system (Cosier & Glazer, 1986) and held at the target temperature for 5 minutes before commencing the data collection (4-35°, 2θ, 0.017° per step, 1 second exposure). For the samples 1,4-dioxane and tetrahydrofuran, the heating process took 30 minutes to increase from 293 K to the next temperature in the series; 343 and 313 K respectively. Material isolated from pyridine and methanol slurries provided XRPD data consistent with that of α-NIF, therefore single crystals of these solvates were grown and ground for capillary XRPD data collection. In all cases, unit cell parameters were determined over the range of temperatures for each solvated structure using Rietveld refinement through the Topas software in the batch processing sequential mode (Topas Academic V5).(Coelho, 2018) The fitting of the patterns near the transition were revisited due to the automated procedures not coping with the multiple phases and the unit cell parameters used in the plots.

For the low-temperature phase of the DMA solvate, the powder pattern (100 K data) was indexed using DICVOL06 (Boultif & Louër, 2004) in DASH (David et $al.$, 2006) to give unit cell parameters, a = 7.83743(13) Å, b = 12.6144(2) Å, c = 13.2163(3) Å, α = 62.9281(19)°, β = 74.129(2)°, γ = 64.8735(17)°. From these parameters, the content of the asymmetric unit was calculated to be one molecule of NIF and one molecule of DMA. The structure was solved from the X-ray powder diffraction data using simulated annealing (DASH). Rietveld refinement of the new polymorph against the low-temperature powder data was performed using Topas Academic (R_{wp} = 3.85%). The refinement indicated some fraction of the high-temperature phase remaining at 100 K (5%).

2.5. Thermal analysis

Differential Scanning Calorimetry (DSC) and Thermal Gravimetric Analysis (TGA) were carried out using the STA 449 F1 Jupiter. Samples (ca. 4-6 mg) were loaded into aluminium pans with pierced lids and sealed. The temperature programme was as follows: 20-minute isothermal step (293 K), heat (293-493 K, 10 K/min), cool (493-293 K, 10 K/min) and a final isothermal step for 5 minutes (293 K). Helium was used as a purge and protective gas at a rate of 50 ml/min and 20 ml/min respectively. Data was analysed using NETZSCH Proteus Thermal Analysis 8.0.2.

2.6. FT-IR spectroscopy

From our experiments, the crystallisation behaviour of nifedipine from methanol and ethanol is different therefore FT-IR was used to assess the molecular structure in solution to see if there was any difference between the two solutions. The filtered supernatant solution collected after slurrying was analysed prior to crystallisation. FT-IR spectra were collected using a Shimadzu IRSpirit Fourier Transform Infrared Spectrophotometer with QATR-S single-reflectance attenuated total reflectance (ATR) probe. Parameters for data collection were transmittance measurement mode and Happ Genzel apodization. Spectral resolution was set to 4 cm^{-1}, with 64 scans per spectrum in the range of 400 to 4000 cm^{-1}. Background scans of the solvent were conducted between each sample to remove spectra of the pure solvent.

3. Results and Discussion

Before we discuss the solvate formation in NIF, it is informative to discuss its polymorphism. There are inconsistencies in the nomenclature of NIF in the literature, so to clarify, we will be using the Greek letter notation of the phases. Table 1 provides a breakdown of the nomenclature in use in the literature and how the notations relate to one another. The α-form (Form A) was first solved by Triggle *et al.* and is the thermodynamically stable form before melting.(Triggle *et al.*, 1980) The β-, γ-, and δ- forms can all be isolated from the melt. The β-form (Form C) is produced by crystallisation of the liquid state created by heating the amorphous form. The initial determination of the crystal structure was via synchrotron X-ray powder diffraction (Bortolotti *et al.*, 2011) before subsequent confirmation using single-crystal X-ray diffraction.(Gunn *et al.*, 2012) Two further polymorphs of NIF were discovered by Gui *et al.* by varying the crystallisation conditions and temperature.(Gui *et al.*, 2020) The high temperature β'-form is accessed by heating the β-phase above 333K, indicating their enantiotropic relationship. The γ'-form is observed by crystallisation of the melt at 373 K. Single crystals of this polymorph can be grown by annealing the solid near its melting point (410 K). One of the key observations is that it, so far, it can only be observed from isolated liquid droplets and converts readily to the other forms on contact with those crystals.(Gui *et al.*, 2020) The relationship

6

with its parent structure (γ-form) is also enantiotropic and the reversible conversion to the γ-form occurs at 243 K. Finally, the δ-form was crystallised in a two-step process by seeding the melt of NIF with structurally similar compound felodipine then subsequently using the powder of the δ-form to seed droplets of the NIF melt. The use of felodipine enabled NIF to possess the *cis/cis* conformation not seen in the other polymorphs. The unit cell parameters for each of the known forms are in Table S1. From these observations it would seem likely that the α-, β-, β'-, and γ'-forms are likely candidates for the desolvation product.

Table 1   Nomenclature of the nifedipine polymorphs and their relationship between the different literature sources as well as the two known solvates of nifedipine.

Burger & Koller, 1996	Grooff *et al.*, 2007, 2011	Gunn *et al.*, 2012	Gui *et al.*, 2020
I	Form A	α	A
II	Form B	β'	β'
III			γ' then γ @ 247 K
	Form C	β	B
		X†	

Solvates of nifedipine	
Klimakow *et al.*, 2010	Caira *et al.*, 2003
DMSO	Dioxane

†Identified through powder diffraction but no further characterisation has been done nor phase observed in studies to date.

NIF is a dihydropyridine compound that has shown propensity to form solvate structures. Solvents selected for this study were based on the two NIF solvates deposited in the Cambridge Structural Database (CSD): 1,4-dioxane (N_{14DIO}; CSD Refcode: ASATOD)) and dimethylsulfoxide (N_{DMSO}; CSD Refcode: QUPRUP).(Groom *et al.*, 2016; Klimakow *et al.*, 2010; Caira *et al.*, 2003) NIF solvates were produced from various solvent systems: morpholine, tetrahydrofuran, pyridine, dimethylacetamide (2 polymorphs), dimethylformamide and methanol, in addition to the known 1,4-dioxane and dimethylsulfoxide structures. The remaining solvents recrystallised the thermodynamically stable α-NIF from slow evaporation and slurry routes (Figure S1).

3.1. Structural similarity

7

In the solvent screen component of this study 7 new solvated structures were obtained and the rest of this section will describe and discuss these. The new structures can be split in to two different groups; (i) those that are structurally similar to the known N_{14DIO} and N_{DMSO} structures, and (ii) those that are significantly different to the previously known solvated forms. One of the key structural observations is that the conformation of the nifedipine, in all but the methanol and pyridine solvates, is the same *cis*/*trans* configuration. In the methanol and pyridine structures the acetate groups are orientated in the *cis/cis* configuration, making the molecules symmetrical. The conformational changes alter the interaction with the solvent molecules and the propagation of the crystal structure.

Of the seven new solvated systems, there are three crystals that show structural similarities to the known dioxane and dimethylsulfoxide solvated forms. The similarity is centred around the packing of the NIF molecules with the solvent molecules varying the size of the repeating unit. The THF, pyridine and methanol solvates all crystallise in different packing arrangements, but all show intriguing behaviour that will be discussed in the next section.

### 3.1.1. Dioxane, N_{14DIO} & Morpholine, N_{MORPH}

The crystal structure of the 1,4-dioxane solvate was first described by Caira and co-authors (CSD Refcode: ASATOD).(Caira *et al.*, 2003) The morpholine solvate is isostructural with the dioxane solvate where the asymmetric unit consists of one molecule of NIF and half a molecule of 1,4-dioxane (or morpholine) leading to a 2:1 solvate. In the case of morpholine, the molecule is disordered over the inversion centre with the NH group replacing one of the oxygen atoms. There is no significant change in geometry due to the extra hydrogen bond capability, but the NH group does point towards the nitro group of a neighbouring NIF. The solvent molecule takes a chair conformation and is bonded to the dihydropyridine group of the NIF via a NH···O hydrogen bond parallel to the *b*-axis. The main body of the NIF molecule lies approximately on the (2 1 0) plane with the nitrophenyl group lying perpendicular to this (88.59° for N_{14DIO} and 87.62° for N_{MORPH}). The solvent molecule in each of the solvates is orientated perpendicular to the NIF backbone (Figure 1a). In each of the hydrogen bonded units, the NIF molecules are related by the inversion centre that causes there to be layers in the structure (indicated by the grey- rectangles in Figure 1a). The layers are stacked perpendicular to the *a*-axis with nothing more than van der Waals interactions between the neighbouring layers.

3.1.2. Dimethyl sulfoxide, N_{DMSO}

Despite the obvious differences in the molecular structure of the solvent, the next three structures show significant similarity to the N_{14DIO} and N_{MORPH} structures. The structure of N_{DMSO} was previously determined by Klimakow and co-authors (CSD Refcode: QUPRUP).(Klimakow *et al.*, 2010) It crystallises in *P*-1 with one NIF and one DMSO molecule in the asymmetric unit. Hydrogen bonding connects the two components between the dihydropyridine nitrogen of NIF and oxygen of the DMSO

8

(D⋯A, N2H2⋯O7) with a distance of 2.8597(18) Å compared with 2.877(2) Å observed in the
ambient structure. Interestingly, the DMSO molecules are arranged in an anti-parallel arrangement via
the inversion centre which enables the DMSO to take a similar position in the structure as the dioxane
molecules leading to the similarity in the structures (Figure 1c) albeit that the unit cell volume is
expanded. There are no strong hydrogen bonding interactions between the layers but the orientation of
the nitrophenyl groups enables weaker CH…O interactions to occur with oxygen atoms from the
methoxy group (O5) and nitro group (O1) of a neighbouring molecule, translated down the a-axis.
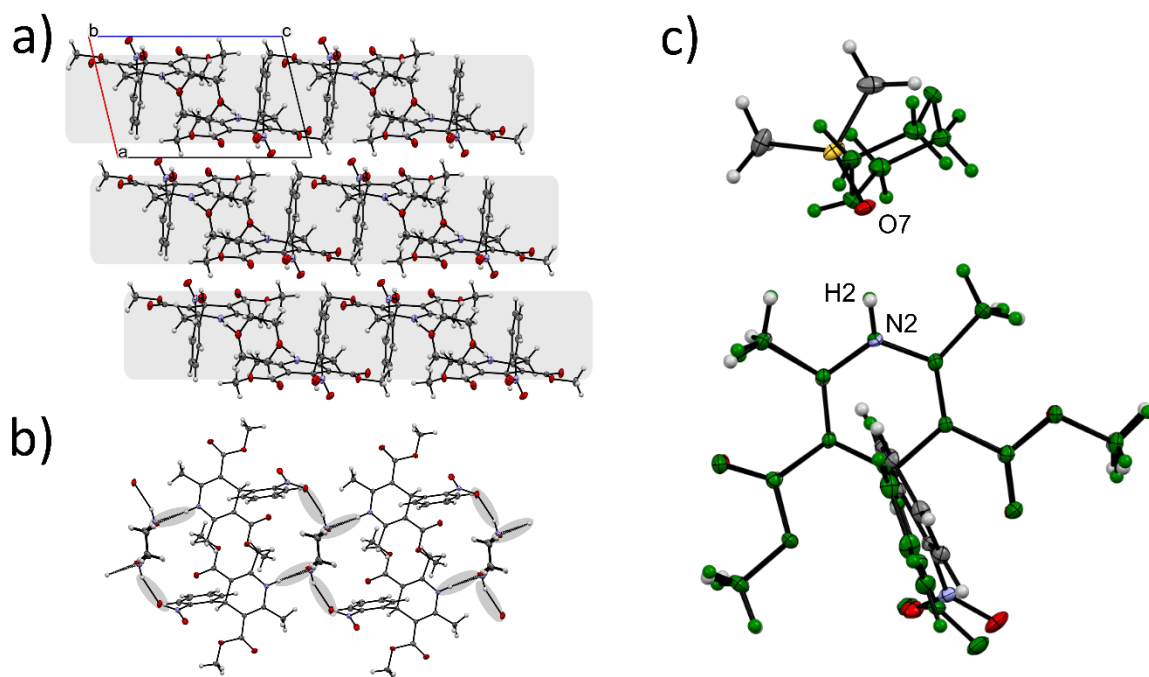
Figure 1 a) Structure of N_{14DIO} shown down crystallographic b-axis. Layers are seen in the structure,
parallel to the c-axis and perpendicular to the a-axis highlighted in the figure. Nitrophenyl groups
separate the layers that run perpendicular to the a-axis. b) The isostructural morpholine solvate within
the isostructural solvate in both of the modelled orientations, forming a ring structure. c) Overlay of
the N_{MORPH} (green) and N_{DMSO} (coloured by element) solvates, highlighting the similarity in the
position of the solvent molecules in the structure when the main bodies of the nifedipine are overlaid.

3.1.3. Dimethylacetamide, N_{DMA}

Whilst N_{DMSO} has a unit cell that is broadly similar to the N_{14DIO} structure, the dimethylacetamide
solvate forms a structure that is elongated along the c-direction; this can be attributed to the location
and orientation of the solvent molecules. N_{DMA} undergoes a phase transition on cooling below 143 K
into a low temperature phase. We have denoted the high temperature phase α-N_{DMA} and the low-
temperature phase β-N_{DMA}. To characterise α-$N_{DMA,}$ single crystal diffraction data was collected at 173
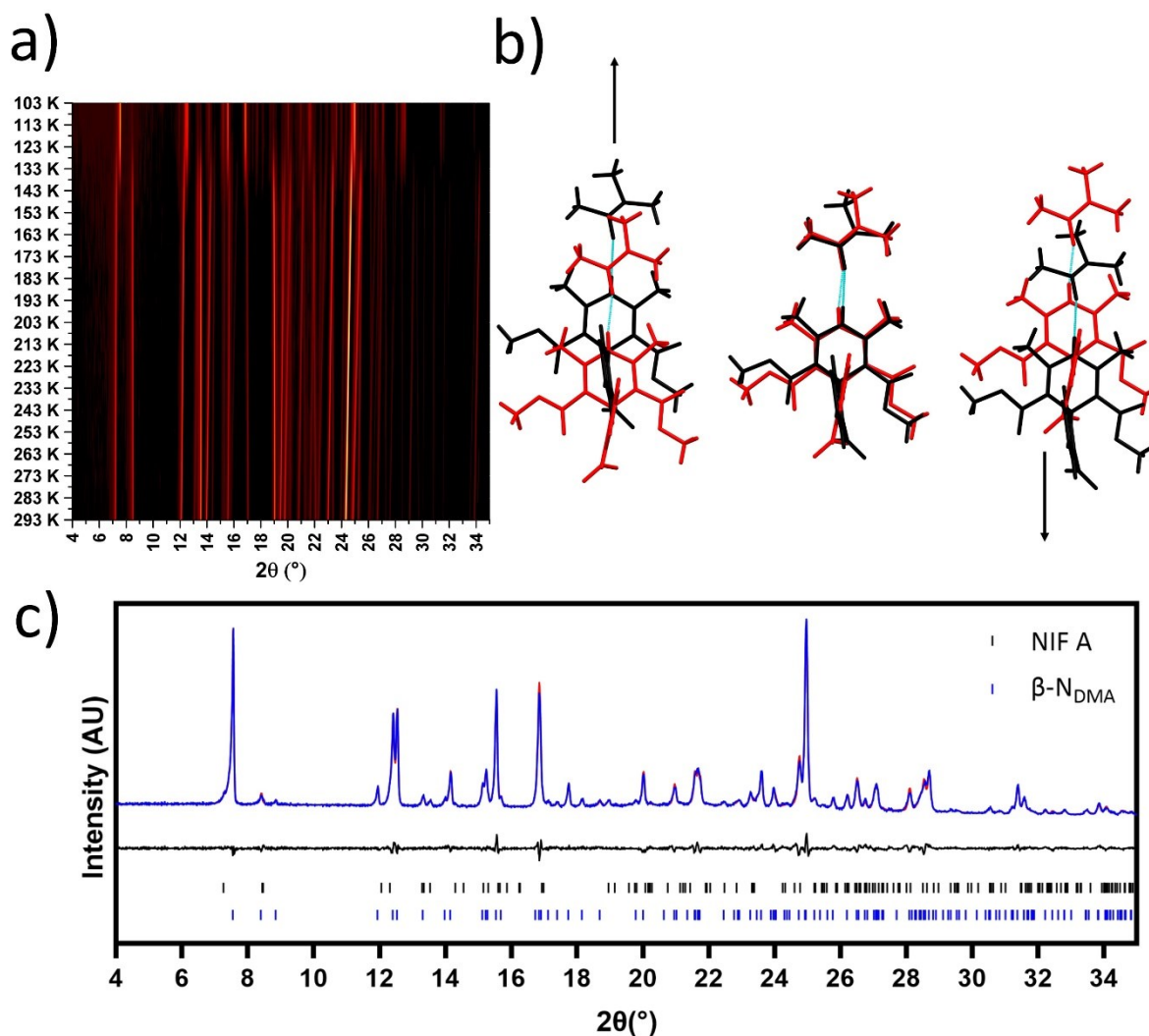K to avoid the phase transition.

9

The hydrogen bonding is consistent with the other solvated forms and via the NIF dihydropyridine group. The main body of the NIF molecules sit on (101) plane with weak CH…O interactions with the nitro group between the layers of NIF molecules. The DMA molecule sits planar with respect to the dihydropyridine ring of NIF (6.80° between the mean plane of the DMA and dihydropyridine ring) and the other solvent molecules in the channel, with little interaction between them. The DMA molecule shows disorder, occupying two positions in the structure. The shape of DMA enables the solvent molecule to adopt two positions without a significant change in occupied space (Figure 2, inset). The methyl groups that are trans to one another can "swap" positions whilst maintaining the hydrogen bonding interaction to the carbonyl oxygen.
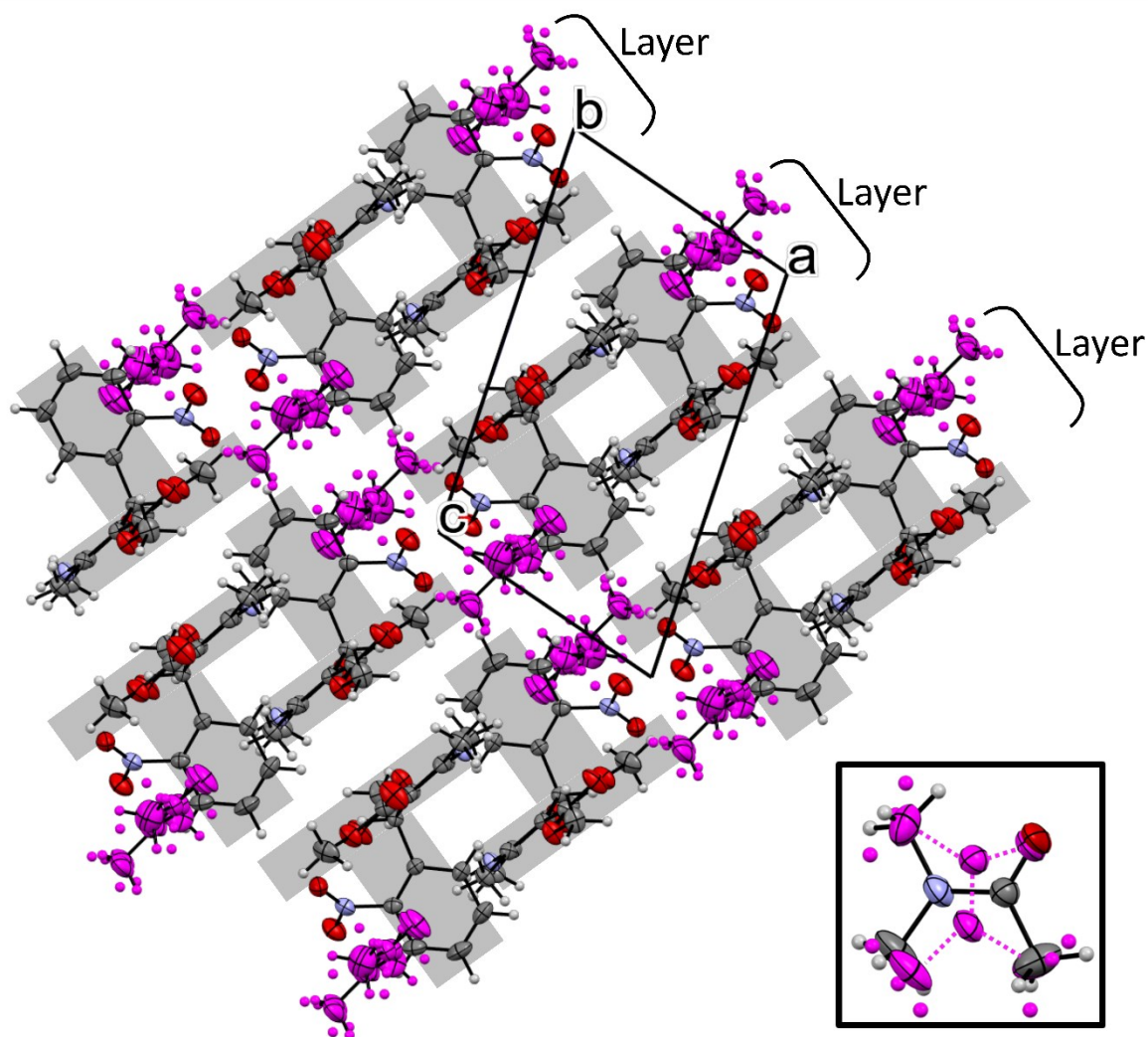
Figure 2 Layers in the N_{DMA} structure. Nitrophenyl groups are orthogonal to the main body of the nifedipine, fitting in the opposite chain forming a bilayer, forming a T-motif. DMA molecules are coloured pink for visual ease. Inset shows the two orientations DMA occupies in the structure, coloured in pink and by element.

10

Whilst mounting a crystal of N_{DMA} onto the diffractometer with the low temperature device operating at 100 K, the single crystal turned opaque and disintegrated indicating a phase transition had occurred. The reconstructive nature of the transition necessitated the use of powder diffraction to elucidate the structural changes over the transition. A freshly ground sample of N_{DMA} was loaded into a capillary to provide the best quality powder diffraction patterns with minimal chance of the pattern being affected by preferred orientation. Figure 3a shows the surface plot of the XRPD data captured every 10 K from 293 K down to 103 K indicating that a phase transition does occur at 143 K and that β-N_{DMA} remains stable to 103 K. The XPRD pattern reversibly converts back to the α-NIF_{DMA} pattern on return to ambient temperature. The crystal structure of β-N_{DMA} was solved using the X-ray powder diffraction data and found to have a stoichiometric ratio of 1:1 NIF: DMA, maintaining the ratio from α-N_{DMA} but with an ordered solvent molecule. β-N_{DMA} possesses unit cell parameters that are very close to the original phase with a significant change in the γ-angle.

The overall packing of the structure of β-N_{DMA} is significantly different to the α-form with 2 out of 15 molecules identified as being common using the packing similarity methodology in the Mercury.(Macrae *et al.*, 2020) The two phases maintain a similar hydrogen-bonding motif but the arrangement of the molecules in the layer is different (Figure 3b). On cooling to 100K, neighbouring units of NIF and DMA (~along *b*-axis) move in opposite directions along the hydrogen bond (moving from red arrangement to black arrangement in Figure 3b). The group to left of the central unit moves upwards whilst the group on the other side moves downwards in the same plane. During this transition, there is a slight conformational change around the nitrophenyl group of NIF and the DMA molecules no longer lie parallel with the NIF backbone. Whilst the difference of the two structures seems to be relatively small, the lateral movement of all the hydrogen-bonded units is catastrophic for the integrity of the crystal.

Figure 3 a) the XRPD patterns as a function of cooling indicating the emergence of the β-phase at 143K; b) the change to the structure from α-N$_{DMA}$ (red) to β-N$_{DMA}$ (black) over the phase transition. The NIF molecules remain in the same plane but move laterally along the direction of the hydrogen bond; c) Rietveld refinement of pattern collected at 103 K using the structure solution for β-N$_{DMA}$ obtained from powder data (experimental pattern – red, model – blue, difference – black). A minor contribution from NIF A was also identified in pattern, *hkl* tick marks for the component phases are shown as vertical bars (black – NIF A, blue – β-N$_{DMA}$)

3.1.4. Dimethylformamide, N$_{DMF}$

N$_{DMF}$ shares structural similarities to α-N$_{DMA}$ with 6/15 molecules overlapping after conducting a structure similarity search in Materials Mercury, (Macrae *et al.*, 2020) but we note that there is a difference in collection temperature (100 K vs 143 K). This indicates that just under half of the molecules are located in a similar position between these two phases. At 100 K, β-N$_{DMA}$ shows no overlap with N$_{DMF}$ indicating the large change in the molecular packing between the N$_{DMA}$ forms over

12

the phase transition. In N_{DMF}, we observe the same hydrogen bonding motif (N2H2···O7, 2.8533(12) Å). The DMF molecules reside in a similar location of the structure to the DMA but the DMF molecules sit perpendicular with respect to the main body of the NIF molecules (65.49°). The solvent molecules are not disordered and are fixed in one orientation, sitting in channels parallel to the *a*-axis. In this orientation, the DMF can interact with the methoxy group of the NIF molecules in the layer above and a second symmetry-related molecule interacts from above.

3.2. Thermal Analysis of structurally similar compounds

The focus of the paper was to determine the desolvation process in NIF solvates with a view that we may access the metastable forms. To elucidate the changes on desolvation we used both differential scanning calorimetry and thermogravimetric analysis of the powders in combination with variable-temperature powder X-ray diffraction measurements. For all the structurally similar systems under study, the crystal structures show that on heating the expansion is anisotropic, with greater increase in the *a*-axis which is perpendicular to the layers in the structure where hydrogen bonding is absent. The desolvation for N_{14DIO}, N_{MORPH} is straightforward and clean with a clear transition from the solvate to the α-form of NIF beginning at 373 K and is complete by 408 K (for N_{14DIO}, Figure S2) whilst N_{MORPH} desolvates a little earlier at 358 K with completion by 388 K (Figure S3). The temperature consistent with the observations of the desolvation of N_{DIO} by Caira *et al.*(Caira *et al.*, 2003) There is a small loss of morpholine at 320 K that may suggest some residual surface solvent escaping at this temperature. The solvent molecules are located in channels parallel to the *b*-axis, so it is likely that on thermal expansion, solvent molecules can easily escape the structure. Over the timescale of the XRPD run, there is no indication of amorphisation hence the transition to thermodynamically stable α-form is via the rearrangement of the crystalline phases.

N_{DMSO} and N_{DMA} show slightly different behaviour to the solvates previously described, where both show a significant decrease in the crystallinity of the solid as we approach the melting point of NIF. N_{DMSO} shows a constant mass loss from 293 K towards the maximum temperature reached, 473 K, indicating that there may be some decomposition occurring in solution (Figure S4). The DSC trace of N_{DMSO} is rather unusual and does not look as clean as N_{14DIO} and N_{MORPH}. There is a prolonged endothermic event beginning at 310 K and complete by 350 K that cannot easily be ascribed to any event. VT-XRPD gives us a clearer indication of the change to the crystal structure as a function of the desolvation and indicates that the solvate undergoes a transition to α-NIF at 363 K; the difference in the temperature (compared to DSC) can be attributed to the different sample environments, ramp rates and holding temperatures for the collection of the XRPD data. Consistent with N_{14DIO} and N_{MORPH}, the DMSO molecules are located within channels in the crystal structure which should aid the escape of the solvent.(Liu *et al.*, 2019) In this solvate, we observed that the diffraction patterns

13

near the melt are of poor quality. There is a general reduction in reflection intensity and observation of an amorphous background suggest the melting of the solvate; this is indicated by the increase in the background colour in Figure S4. The lower crystallinity after the melting event and appearance of α-NIF suggests that the DMSO released from the structure stays in the capillary and coalesces as a liquid for the NIF to dissolve and recrystallise. This idea is supported by the DSC trace, where there is a very broad endotherm of NIF rather than the sharp event associated with a melt. N_{DMA} shows complete desolvation by 383 K to α-NIF. The mass loss of 23.61% is equivalent to the mass of DMA indicating that it is a complete process (Figure S5). In a similar manner to N_{DMSO}, there is the appearance of an amorphous structure in the background on desolvation that indicates a similar process where DMA acts as the solvent to dissolve NIF.

N_{DMF} shows interesting behaviour on heating that the other materials have failed to exhibit thus far. The expansion of the unit-cell parameters for the solvate can be fitted up to 348 K, and beyond 363 K they can be fit to α-NIF. Between these temperatures, however, reflections for another form are observed in the VT-XRPD. (Figure 4). These reflections cannot be attributed to any of the metastable forms of NIF (Figure S6). From the VT data, the X-ray pattern at 358 K provided the best opportunity to solve the new phase. This pattern displays some diffraction that can be attributed to α-NIF but this is present at a low level. Using Topas, we were able to identify those diffraction intensities that were attributable to both α-NIF and N_{DMF} and discount these from our list of reflections for indexing (the latter was not present). The other unindexed peaks were identified and used to index the unknown phase. After numerous attempts in DASH,(David *et al.*, 2006) Topas (Coelho, 2005) and N-TREOR,(Altomare *et al.*, 2000) a consistent unit cell was identified (a = 15.436400 Å, b = 15.20191 Å, c = 9.50456 Å, 90°, 98.3578°, 90°) in space group $P2_1$. The Pawley fit to the data using this cell is good with a R_{wp} 10.17 for the mixed phase (Figure 4e) The volume of 2205 Å^3 indicates that the structure contains two molecules of NIF and two molecules of DMF based on the 18 Å^3 rule (i.e., each non-H atom has a volume of 18 Å^3). Attempts were made to solve the structure in DASH,(David *et al.*, 2006) FOX (Favre-Nicolin & Černý, 2002) and EXPO (Altomare *et al.*, 2013) using both $P2$, $P2_1$ and $P2_1/m$ but no satisfactory solution was found albeit that the chi^2 values were promising. The lack of structural solution for this additional phase (designated β-N_{DMF}) is frustrating but from the analysis that we have performed it appears that the phase transition is a change in polymorph rather than a loss of solvent. The thermal identification of this transition is complicated by the fact that the transition is close in temperature to the desolvation temperature hence is masked in the thermal analysis (assuming the conversion occurs in the DSC/TGA under slightly different heating parameters). The TGA indicates there are two different weight loss events the first of which is a continuous weight loss of 15.01% before a second discrete loss of 1.97% released on melting (Figure 4c & Table 2). The calculated weight loss for the desolvation for a 1:1 NIF:DMF solvate is 17.43% which confirms the total loss during the experiment (16.98%).

14
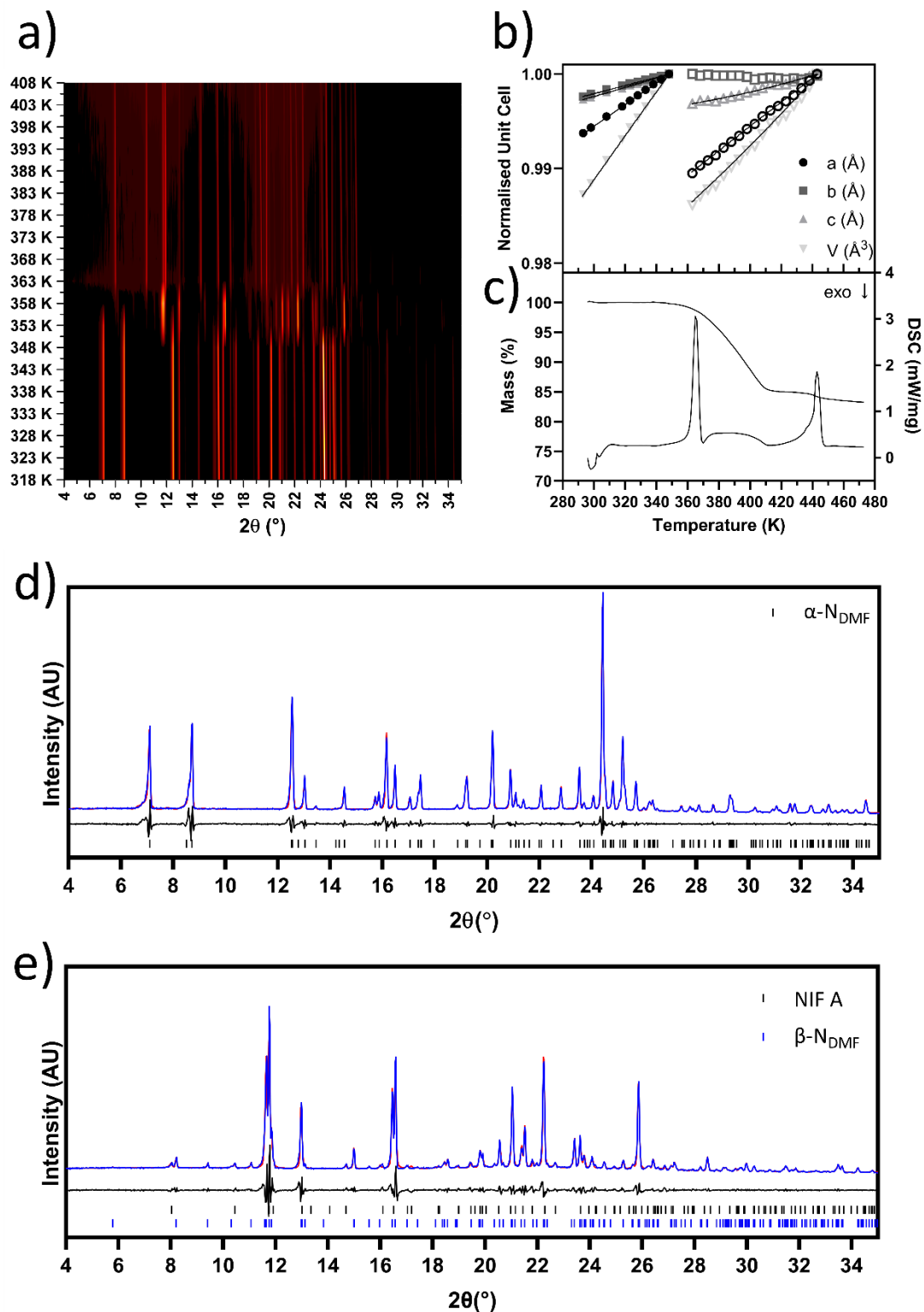
Figure 4 Thermal data of N_{DMF} capturing the desolvation to α-NIF a) Surface plot of VT-XRPD data from 318 K to 408 K. b) Unit cell parameters from Rietveld refinements of each XRPD pattern. Closed symbols represent data for the solvate; open symbols represent data for desolvated structure. The data is fit with the Berman 1988 Equation of State.(Angel *et al.*, 2014; Gonzalez-Platas *et al.*,

15

2016; Berman, 1988) c) DSC and TGA trace for N_{DMF}. d) XRPD pattern for the DMF solvate collected at 293 K (the model (blue) is superimposable on the data (red) indicating a good fit). e) XRPD pattern obtained at 358K (after phase change). The pattern is well accounted for by indexed phase (β-N_{DMF}) and minor component of NIF A. For both fitted pattern (d, and e), the experimental data is shown in blue, whilst the calculated profile is shown in red. The difference profile is displayed underneath the diffraction pattern.

Table 2   Thermal analysis data for NIF solvates.

Solvate	Expected Mass Loss (%)[a]	Observed Mass Loss (%)[b]	Onset Temperature of desolvation (K)	Enthalpy of desolvation (kJmol^{-1})	Boiling point of Solvent (K)
N_{14DIO}	11.28	8.07	392.1	19.28	374
N_{MORPH}	11.17	11.81	378.1	19.58	402
N_{THF}	9.43	9.48	349.2	21.41	339
N_{PYR}	18.59	17.06	325.8	35.40	388
N_{DMSO}	18.41	32.47	320.9	23.00	462
N_{DMA}	20.10	23.61	369.3	57.39	438
N_{DMF}	17.43	16.98	362.2	30.85	426
N_{MeOH}	8.47	1.69	328.9	9.78	338

[a] Calculated from SC-XRD data. [b] Calculated from TGA data.
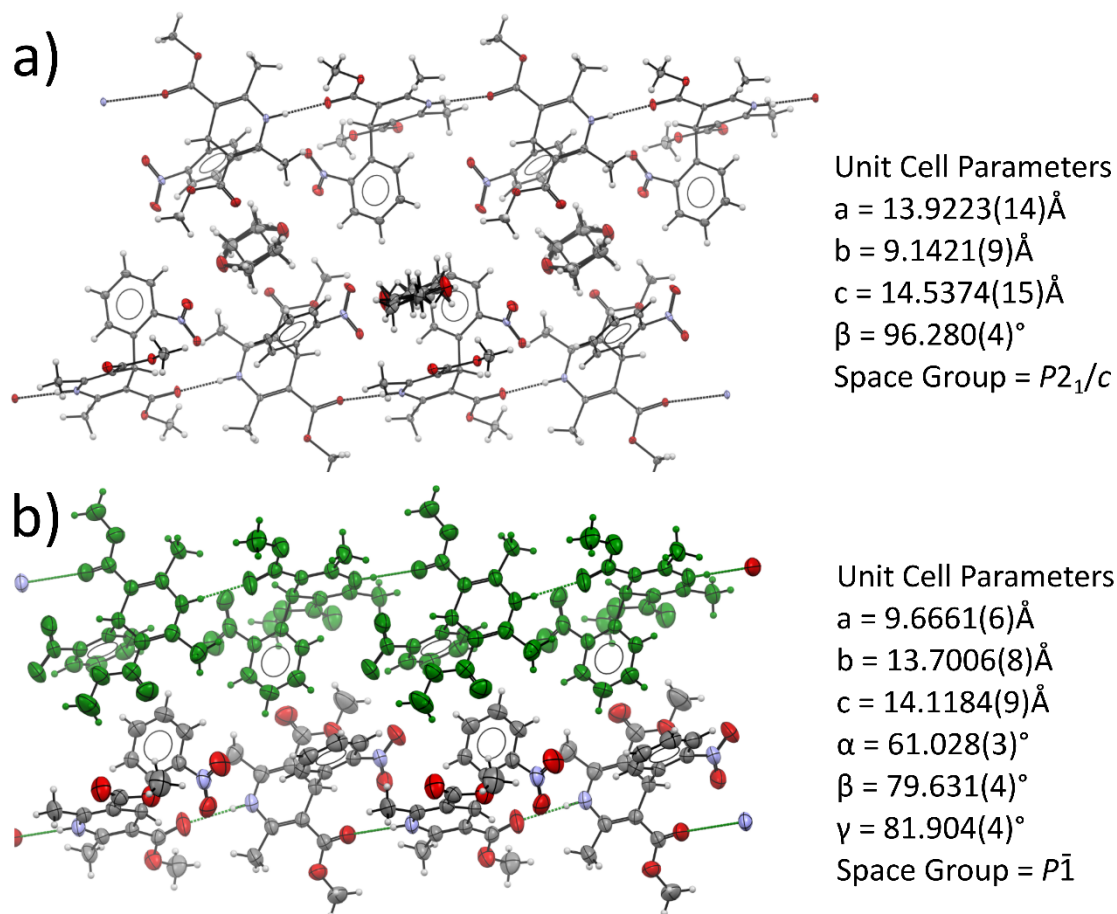
3.3. Unique solvate structures

3.3.1. Tetrahydrofuran, *N_{THF}*

Tetrahydrofuran (THF), a cyclic ether, can form one hydrogen bond via its oxygen atom. Although collected at 100 K, the modelled structure showed disorder, with the solvent molecules sitting on an inversion centre despite not being centrosymmetric which would open up the potential for hydrogen bonding in opposite directions (Figure 5). Despite this, the THF is not involved in any hydrogen-bonding interactions at all. NIF molecules form hydrogen bonds between the nitrogen in the dihydropyridine (N2) and the ester carbonyl group of a neighbouring molecule (O6) that resembles the metastable polymorph of NIF, β-form (Figure 5). The unit cell parameters and the hydrogen bonding in this structure are similar to β-NIF but the NIF molecules are symmetry-equivalent in N_{THF}. The differences between N_{THF} and the β-form of NIF show that there is a translational change in the neighbouring chains that allows the THF to sit in pockets between the chains made by the nitrophenyl rings. There are no opportunities in this pocket for the THF molecules to engage in hydrogen bonding.

16

The addition of the THF into the structure has altered the O2 N1 C1 C2 dihdral angle from 143.29° and 151.77° in molecules 1 and 2 of the β-form to 133.21° in the N_{THF} structure.

a)

Unit Cell Parameters
a = 13.9223(14)Å
b = 9.1421(9)Å
c = 14.5374(15)Å
β = 96.280(4)°
Space Group = $P2_1/c$

b)

Unit Cell Parameters
a = 9.6661(6)Å
b = 13.7006(8)Å
c = 14.1184(9)Å
α = 61.028(3)°
β = 79.631(4)°
γ = 81.904(4)°
Space Group = $P\bar{1}$

Figure 5 The similarities in the hydrogen bonding chains in a) N_{THF} and b) β-form of NIF indicating the similarity. Neighbouring chains are translated to accommodate the THF molecules in the structure. The green colouring of β-form to highlight the neighbouring chain. Both structures were collected at 100 K. The unit cell parameters for the β-form have been taken from the CSD (refcode: BICCIZ02) and transformed to equate to the N_{THF} solvate which shows the commonality in the unit cell lengths.(Groom *et al.*, 2016)

In N_{THF}, the expansion of the structure is greatest in the direction of the *a-* and *b-* axes where there is no hydrogen bonding present. These axes exhibit identical behaviour (Figure S7). The DSC indicates that desolvation takes place between 349 and 361 K, above the boiling point of THF at 339 K, with a single desolvation event. There is some discrepancy between the DSC and VT-XRPD where the diffraction indicates that the desolvation starts to take place as early as 313 K. This can be attributed to the differences in the experimental process e.g., grinding the powder before XRPD analysis and sample holder i.e., aluminium pan versus borosilicate capillary. The process of grinding the sample is likely to have the greatest impact, imparting energy into the material and increasing the surface area for quicker desolvation. From the Rietveld analysis of the data collected at 323 K, additional peaks of

17

the α-form of NIF were observed. N_{THF} is present in detectable quantities until 348 K where the conversion is complete; the unit cell parameters can only be fitted up to 338 K due to the low level of the N_{THF} present in the sample beyond this temperature. From the BFDH morphology prediction of the crystal shape, the THF molecules reside in layers on the largest face of the crystal surfaces that would facilitate the desolvation (Figure S7). Although N_{THF} and β-form NIF are structurally similar, we do not see reflections corresponding to β-form during the desolvation. This is somewhat surprising given the structure of the solid. However, Grooff *et al.,* observed that the β-form easily converts to thermodynamically stable α-form of NIF via the metastable Form β' at approximately 343 K (Grooff *et al.*, 2007) on heating which would be consistent with our observations. TGA data can also be used to confirm the stoichiometry of the crystal structure that is provided by single-crystal XRD. The calculated ratio of NIF to THF is 2:1, with a weight loss of 9.43% after desolvation, which agrees with the experimental data (9.48%).

3.3.2. Pyridine and Methanol

Pyridine N_{PYR}

The asymmetric unit of N_{PYR} contains two NIF and two pyridine molecules. This solvate crystallises in $P2_1$ with unit cell lengths of 9.4363(10) Å, 14.4247(14) Å and 15.1387(15) Å for *a*, *b*, and *c* respectively, and a β angle of 96.16°. NIF interacts through the dihydropyridine and the pyridine nitrogen with the main body of the NIF molecule lying parallel to the pyridine (red and blue, yellow and green). These symmetry inequivalent pairs stack in an anti-parallel manner at a distance just beyond the van der Waals radii of the atoms (Figure 6). The pyridine molecules are located in small pockets, sandwiched between the methoxy group of a molecule translated along the *a*-axis and ring system of the second NIF molecule in the asymmetric unit. As we extend out along *c*-axis, the close contacts between the nitro groups and neighbouring methoxy group become evident.

18
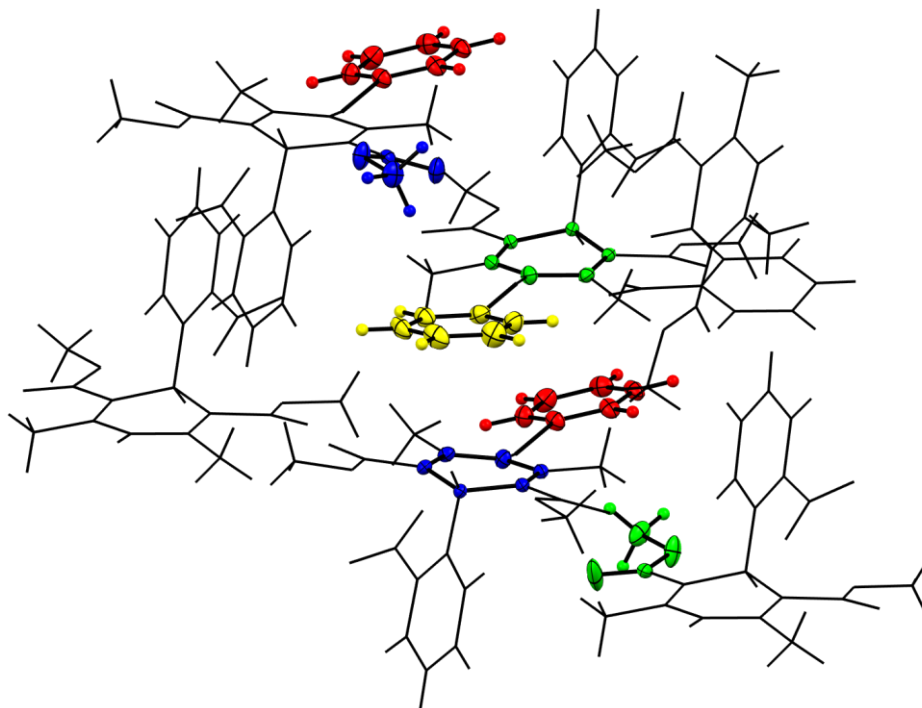
Figure 6 Structure of N_{PYRI} indicating the anti—parallel stacking of the pyridine molecules with the dihydropyridine ring system of NIF. The pyridine molecules are sandwiched between dihydropyridine ring and methoxy group of a neighbouring molecule. Colour scheme is by symmetry equivalence.

Interestingly, the diffraction patterns produced for pyridine via the slurry method showed the sample to be α-NIF indicating that the pyridine solvate is likely to be the metastable form. Therefore, we needed to change our method to produce the powder for desolvation analysis. Single crystals produced by slow evaporation were ground into the powder which may have affected the desolvation process through the extra manipulation of the solid during the preparation of the powder. During VT-XRPD studies, N_{PYRI} shows noticeable expansion in the *b*-axis, the direction perpendicular to the layers within the crystal structure, where there is only π-π interactions between molecules. The desolvation of the sample is rapid, with full conversion to the α-form of NIF by 323 K. Unit cell parameters could only be determined between 293 and 313 K but with the limited data, it suggests that the expansion is anisotropic. DSC for N_{PYRI} shows desolvation of the system has an onset of *ca*. 304 K and is complete by *ca.* 352 K, below the boiling point of pyridine (388 K) (Figure S8). The DSC graph shows a structured endotherm, with overlapping peaks observed during desolvation which can be attributed to the different symmetry-inequivalent pyridine molecules being released at slightly different times. The TGA indicates that the release is continuous with some variation in the rate as opposed to the distinct two-step desolvation observed in furosemide-THF and furosemide-DMF samples.(Minkov *et al.*, 2014)

19

Methanol N_{MeOH}

The final structure is N_{MeOH} which was an unexpected solvate isolated from the slow evaporation of a methanolic solution. A slurry of NIF in methanol resulted in crystals of the α-form of NIF similar to the N_{PYR}. This seems to be a unique observation of an alcohol system. Previous literature and our own studies did not observe an ethanol or 2-propanol solvate and both crystallised α-NIF.(Li *et al.*, 2020) N_{MeOH} is dissimilar to the solvates reported previously; methanol forms two hydrogen bonds via the hydroxyl group, acting as both donor and acceptor to two NIF molecules (N2H2···O7, 2.9201(11) Å; and O7H7···O6, 2.7995(10) Å). The ability of the methanol to form two hydrogen bonds leads to a chain structure parallel to the b-axis. This hydrogen-bonded chain structure resembles α-NIF, which has hydrogen bonds between a carbonyl group and pyridine of neighbouring molecule (Figure 7). The main body of the NIF is parallel to the (3 0 -2) plane and the chains above and below are linked through an inversion centre with little interaction between layers other than van der Waals interactions. There is little interaction between neighbouring supramolecular columns along the *a*-axis.
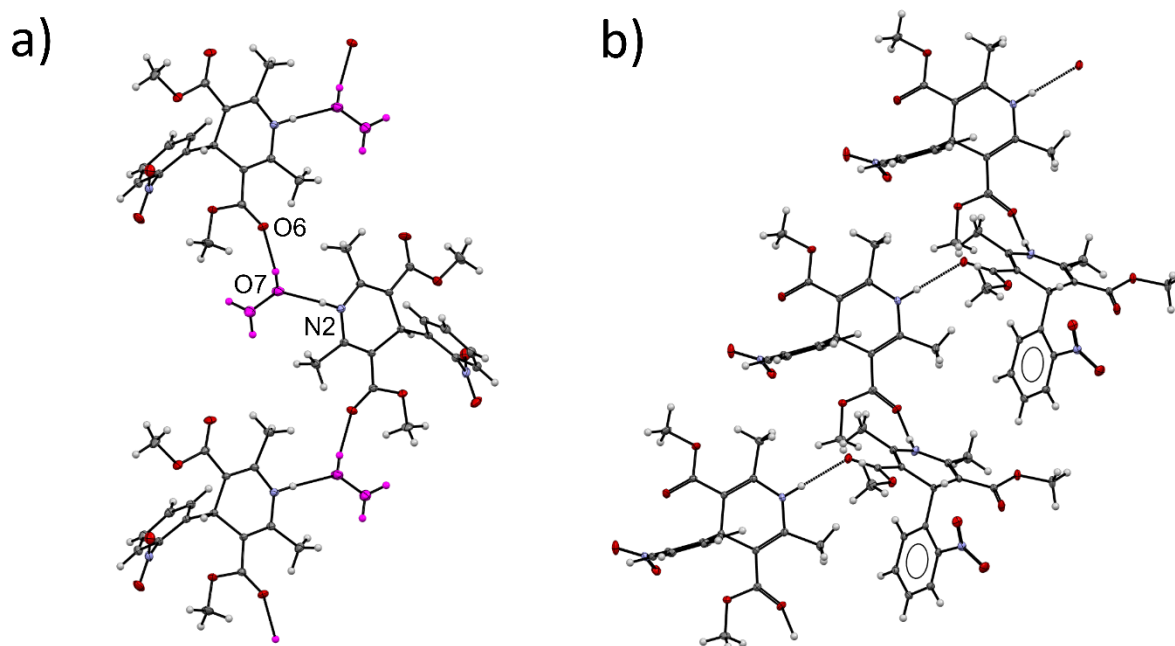

Figure 7 The structure of (a) N_{MeOH} and (b) α-NIF showing the similarities in structure between the two forms. The loss of methanol from the structure would enable the NH…O interaction to form without significant change in the packing.

Similar to N_{PYRI}, the slurry of NIF in methanol did not produce the solvated form, therefore single crystals produced from the slow evaporation of the saturated solution were pulverised for analysis. Interestingly, N_{MeOH} displays negative thermal expansion behaviour along its *b*-axis (Figure S9). Negative thermal expansion (NTE) is a mechanism predominantly reported for metal-organic

20

frameworks.(Goodwin & Kepert, 2005; Wu *et al.*, 2008; Lock *et al.*, 2010) Authors describe the mechanism as having a wine-rack expansion; with expansion in one direction causing contraction in a second direction (Cliffe & Goodwin, 2012). Recent publication by van der Lee and Dumitrescu explains how NTE is common amongst organic crystals, but rarely reported.(van der Lee & Dumitrescu, 2021) In N_{MeOH}, chains of NIF and solvent molecules align in the direction of the *b*-axis, with the hydrogen bonds between methanol and carbonyl group of the NIF (O7H7···O6). When viewed down the crystallographic *a*-axis, the methanol molecules are easily distinguished indicating channels throughout the crystal structure (Figure 8, pink molecules). A possible mechanism of solvent loss is that as temperature increases, the channel structure enables the escape of solvent molecules. The loss of methanol, and its bridging interaction, causes the contraction of the NIF molecules together bridging the gap to form the hydrogen bond between the dihydropyridine and the carbonyl of the ester (observed in α-NIF), which causes the contraction in the *b*-axis (Figure 8). STA indicates that the onset of desolvation took place prior to analysis; TGA shows a mass loss of 1.69% prior to the melt of α-NIF, rather that the ideal value for the solvate of 8.47 % using the stoichiometry determined from the crystal structure. This indicates that the solvent is lost easily and as soon as the crystal is taken out of the solvent.

Further investigation into the negative thermal expansion was conducted using SC-XRD at low temperature as a result of the small window of opportunity at higher temperatures due to desolvation. A single crystal was collected at 100 K with subsequent collections increasing by 25 K (Figure 8b and 8c) and indicate that the NTE behaviour extends from 100 K to the desolvation temperature of 340 K. As the temperature is increased there is a reduction in the *b*-axis but expansion along the *c*-axis that can clearly be observed in the animated .gif in the ESI, at 25 K intervals. There is a slight rotation of the body of the NIF that appears to allow the narrowing in along the *b*-direction. The fact that this still occurs at such low temperatures indicates that the NTE is not associated with the loss of solvent on heating but from a rearrangement of the molecules on warming the sample.

21
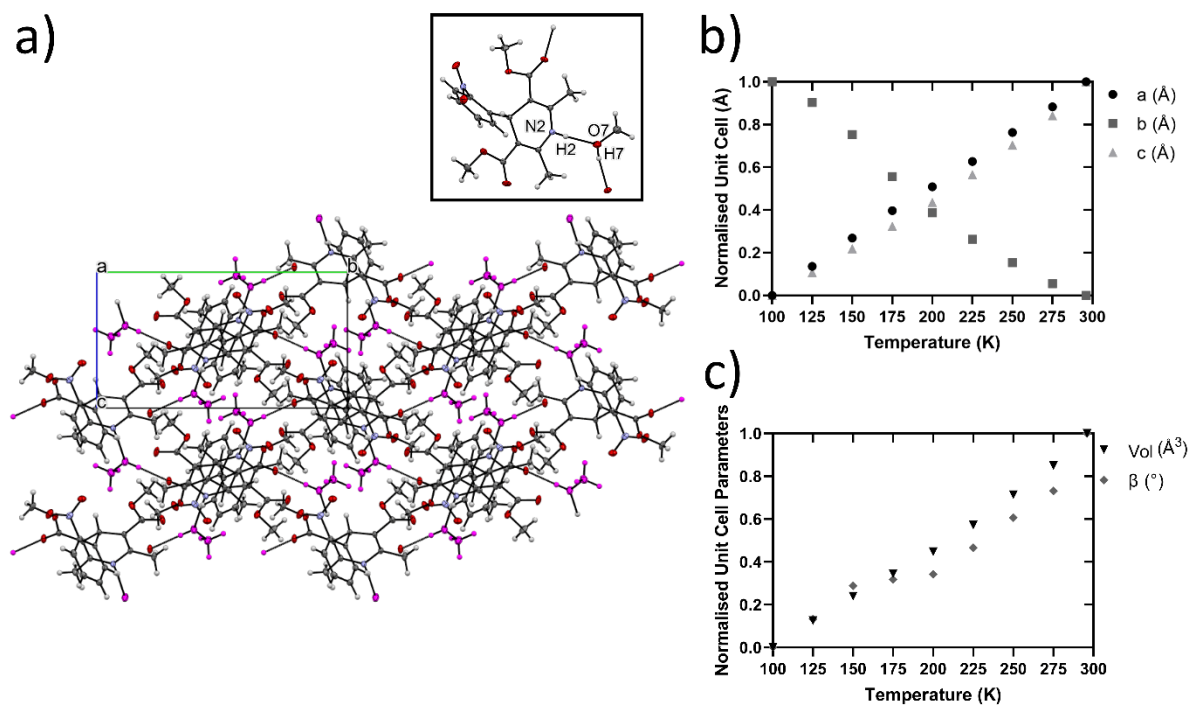
Figure 8 a) N_{MeOH} viewed down the a-axis with methanol molecules displayed in pink residing in the channels parallel to *a*-axis. The inset shows the atoms involved in the hydrogen bonding between methanol and nifedipine. Non-linear thermal behaviour of N_{MeOH} showing the b) decrease in b-axis and c) increase in β angle and volume with increasing temperature.

3.4. Solution Study – Ethanol and Methanol

Despite the successful isolation of a methanol solvate we did not observe a solvate with ethanol. There are a number of reasons behind the difference in the outcomes of the crystallisation. Firstly, the two solvents involved show a variation in rate of evaporation which can affect their ability to be incorporated into the crystal structure. Secondly, the solution structure of the solvent molecules may include clusters of solvent molecules that prohibit the incorporation into the crystal structure. To investigate this scenario further, saturated solutions of NIF in the two solvents were analysed using FTIR. The solubility of NIF in methanol and ethanol at 20 °C are 26 mg/mL and 17 mg/mL respectively.(Ali, 1990) Figure 9 shows the spectra of the filtered saturated solutions, with the background of the respective solvent removed. The IR of NIF was first discussed by Burger and Koller, that helps with the assignment as part of our discussion.(Burger & Koller, 1996) The carbonyl region of the spectra is where differences between NIF in the methanol and ethanol solutions are observed. The IR spectra indicate that the solvent interaction with NIF is causing a change to the carbonyl stretch of the methoxy groups in NIF (regions between 1650-1730 cm^{-1} and 1670-1725 cm^{-1} for methanol and ethanol respectively). The shift to lower wavenumber of the ester stretch can be attributed to the connectivity to the unsaturated bonds in the dihydropyridine ring enabling resonance

22

stabilisation hence a weakening of the stretch. The stretching frequency of the ester group in the ethanol solution is a broader single peak indicating that it is likely composed of two bands with slight differences in energy of the carbonyl group i.e., there is little difference in the intermolecular interactions of each carbonyl group. In methanol, the stretching frequencies of the carbonyl groups significantly changes indicating that the environment around each carbonyl is different. This correlates very well with the observation in the solid-state where the methanol is hydrogen-bonded to one of the ester groups whilst the second ester group is only involved in van der Waals contacts with neighbouring CH groups from the nitrophenyl substituent (Figure S10h). The change in the vibrational behaviour indicates that the interactions could be pre-formed in the solution phase before they are crystallised.(Du *et al.*, 2015) This may account for the difference in the outcomes from the slurry and solvent evaporation routes; the latter providing the opportunity for the interactions to form without the more stable α-NIF being present.
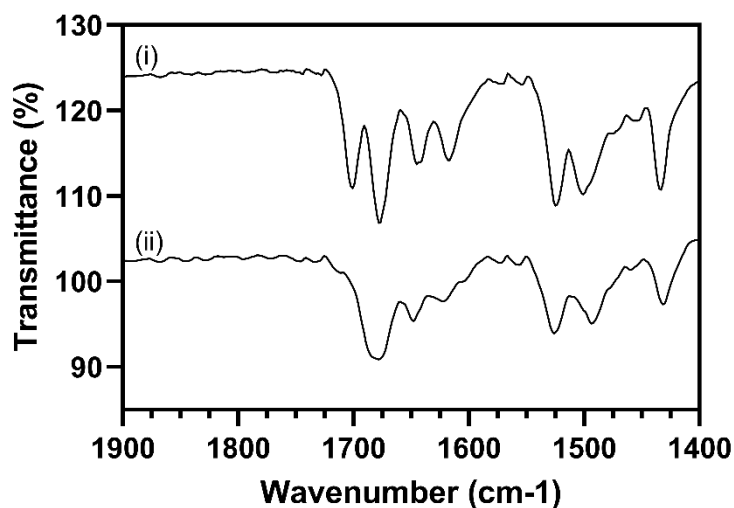
Figure 9 FTIR spectra of NIF in i) methanol and ii) ethanol, between 1400-1900 cm^{-1}, highlighting the region where we see the carbonyl stretch. The background of the respective solvents was removed to aid in the identification of NIF.

3.5. Rationale for solvate formation

The solvents chosen were based on the solvates that had already been identified in the literature (DMSO and dioxane). We believe that the reason for their solvate behaviour is based on several factors. Firstly, for the most part, the solvents only possess hydrogen bond donors that can receive the hydrogen bond from nifedipine, with the solvents used interacting through a hydrogen bond via the amine moiety. Secondly, the size of the solvent molecules also seems to be a feature of these solvates. The successful molecules have a diameter between 5 and 6 Å at their widest point apart from

23

methanol whose diameter is closer to 3 Å. This is important as the dynamic behaviour of molecules during nucleation will be a factor in the successful formation of the crystal. Finally, for those molecules that fit the size range but do not form solvates, e.g. ethanol and 2-propanol, their solution behaviour has been discussed above however another consideration is the packing in the crystal structure. The accepting and donating capability of the alcohol requires a different packing arrangement of nifedipine molecules based on the methanol solvate crystal structure. In this structure, there is no significant space available in the environment around the methyl group of the methanol to enable the insertion of ethanol or propanol without a significant rearrangement of the molecular packing.

4. Conclusion

A solvent screen of NIF has identified seven new solvates, adding to the structural landscape of this pharmaceutical material. The series of solvate structures can be divided into those that are structurally similar to the known dioxane and DMSO solvates (morpholine, DMA and DMF) and those that have their own unique structures (THF and pyridine and methanol). Most of the solvates interacted with the solvent through the dihydropyridine hydrogen-bond donor except for the N_{THF} structure, which possessed a hydrogen-bonding pattern that was similar to the metastable β-NIF. In each case, the hydrogen bonding in the solvates did not substantially affect the outcome of the desolvation process; desolvation gave the known thermodynamically stable α-NIF. We have identified that N_{DMA} and N_{DMF} possess enantiotropically related polymorphs with a reconstructive phase transition occurring between α-N_{DMA} to the low temperature phase β-N_{DMA} at 143 K on cooling, and the transition occurring in N_{DMF} at ~353 K on heating. β-N_{DMA} was solved using the powder diffraction data and shows that the disorder that is present in α-N_{DMA} is resolved on cooling the system; the higher temperature N_{DMF} polymorph remains unsolved but suggests it is a polymorph of the 1:1 solvate. One of the significant findings is that a methanol solvate can be isolated, but an ethanol solvate was not observed. The behaviour in solution indicates that the interaction with methanol molecules is pre-formed in the solution phase before the crystallisation occurs. A rationale for the lack of ethanol solvate could be attributed to the extra methyl group in the solvent that affects the ability to pack into an energetically competitive crystal structure. This study has increased our knowledge of the solid-state landscape of nifedipine but also provided structural information on desolvation routes of these novel phases. This additional information can be vital in the search for novel pathways to polymorphism in pharmaceutical materials.

24

References

Aitipamula, S., Chow, P. S. & Tan, R. B. H. (2011). *CrystEngComm*. **13**, 1037–1045.

Ali, S. L. (1990). Vol. *18*, edited by K. Florey, A.A. Al-Badr, G.A. Forcier, H.G. Brittain & L.T.B.T.-A.P. of D.S. Grady, pp. 221–288. Academic Press.

Altomare, A., Cuocci, C., Giacovazzo, C., Moliterni, A., Rizzi, R., Corriero, N. & Falcicchio, A. (2013). *J. Appl. Crystallogr.* **46**, 1231–1235.

Altomare, A., Giacovazzo, C., Guagliardi, A., Moliterni, A. G. G., Rizzi, R. & Werner, P.-E. (2000). *J. Appl. Crystallogr.* **33**, 1180–1186.

Angel, R., Gonzalez-Platas, J. & Alvaro, M. (2014). *Zeitschrift Für Krist. - Cryst. Mater.* **229**, 405–419.

Berman, R. G. (1988). *J. Petrol.* **29**, 445–522.

Bhardwaj, R. M., Price, L. S., Price, S. L., Reutzel-Edens, S. M., Miller, G. J., Oswald, I. D. H., Johnston, B. F. & Florence, A. J. (2013). *Cryst. Growth Des.* **13**, 1602–1617.

Bodart, L., Prinzo, M., Derlet, A., Tumanov, N. & Wouters, J. (2021). *CrystEngComm*. **23**, 185–201.

Bortolotti, M., Lonardelli, I. & Pepponi, G. (2011). *Acta Crystallogr. Sect. B Struct. Sci.* **67**, 357–364.

Boultif, A. & Louër, D. (2004). *J. Appl. Crystallogr.* **37**, 724–731.

Braun, D. E., Bhardwaj, R. M., Florence, A. J., Tocher, D. A. & Price, S. L. (2013). *Cryst. Growth Des.* **13**, 19–23.

Braun, D. E., Gelbrich, T., Kahlenberg, V., Tessadri, R., Wieser, J. & Griesser, U. J. (2009). *Cryst. Growth Des.* **9**, 1054–1065.

Bruker (2012). SAINT v8.40B. Bruker AXS Inc., Madison, Wisconsin, USA

Burger, A. & Koller, K. T. (1996). *Sci. Pharm.* **64**, 293–301.

Caira, M. R., Robbertse, Y., Bergh, J. J., Song, M. & De Villiers, M. M. (2003). *J. Pharm. Sci.* **92**, 2519–2533.

Cliffe, M. J. & Goodwin, A. L. (2012). *J. Appl. Crystallogr.* **45**, 1321–1329.

Coelho, A. A. (2005). *J. Appl. Crystallogr.* 38, 455-461.

Coelho, A. A. (2018). *J. Appl. Crystallogr.* **51**, 210–218.

25

Cosier, J. & Glazer, A. M. (1986). *J. Appl. Crystallogr.* **19**, 105–107.

David, W. I. F., Shankland, K., van de Streek, J., Pidcock, E., Motherwell, W. D. S. & Cole, J. C. (2006). *J. Appl. Crystallogr.* **39**, 910–915.

Dolomanov, O. V., Bourhis, L. J., Gildea, R. J., Howard, J. A. K. & Puschmann, H. (2009). *J. Appl. Crystallogr.* **42**, 339–341.

Du, W., Cruz-Cabeza, A. J., Woutersen, S., Davey, R. J. & Yin, Q. (2015). *Chem. Sci.* **6**, 3515–3524.

Favre-Nicolin, V. & Černý, R. (2002). *J. Appl. Crystallogr.* **35**, 734–743.

Furuta, H., Mori, S., Yoshihashi, Y., Yonemochi, E., Uekusa, H., Sugano, K. & Terada, K. (2015). *J. Pharm. Biomed. Anal.* **111**, 44–50.

Gonzalez-Platas, J., Alvaro, M., Nestola, F. & Angel, R. (2016). *J. Appl. Crystallogr.* **49**, 1377–1382.

Goodwin, A. L. & Kepert, C. J. (2005). *Phys. Rev. B*. **71**, 140301.

Grooff, D., Liebenberg, W. & De Villiers, M. M. (2011). *J. Pharm. Sci.* **100**, 1944–1957.

Grooff, D., De Villiers, M. M. & Liebenberg, W. (2007). *Thermochim. Acta*. **454**, 33–42.

Groom, C. R., Bruno, I. J., Lightfoot, M. P. & Ward, S. C. (2016). *Acta Crystallogr. Sect. B*. **72**, 171–179.

Gui, Y., Yao, X., Guzei, I. A., Aristov, M. M., Yu, J. & Yu, L. (2020). *Chem. Mater.* **32**, 7754–7765.

Gunn, E., Guzei, I. A., Cai, T. & Yu, L. (2012). *Cryst. Growth Des.* **12**, 2037–2043.

Kaur, N. & Suryanarayanan, R. (2021). *J. Pharm. Sci.* **110**, 3743–3756.

Klimakow, M., Rademann, K. & Emmerling, F. (2010). *Cryst. Growth Des.* **10**, 2693–2698.

van der Lee, A. & Dumitrescu, D. G. (2021). *Chem. Sci.* **12**, 8537–8547.

Li, W., Shi, P., Du, S., Wang, L., Han, D., Zhou, L., Tang, W. & Gong, J. (2020). *J. Cryst. Growth*. **552**, 125941.

Liu, X., Tang, C. C., Boldyreva, E. V & Pulham, C. R. (2019). *Cryst. Growth Des.* **19**, 7315–7323.

Lock, N., Wu, Y., Christensen, M., Cameron, L. J., Peterson, V. K., Bridgeman, A. J., Kepert, C. J. & Iversen, B. B. (2010). *J. Phys. Chem. C*. **114**, 16181–16186.

Macrae, C. F., Sovago, I., Cottrell, S. J., Galek, P. T. A., McCabe, P., Pidcock, E., Platings, M., Shields, G. P., Stevens, J. S., Towler, M. & Wood, P. A. (2020). *J. Appl. Crystallogr.* **53**, 226–235.

Marjo, C. E., Bhadbhade, M., Hook, J. M. & Rich, A. M. (2011). *Mol. Pharm.* **8**, 2454–2464.

Minkov, V. S., Beloborodova, A. A., Drebushchak, V. A. & Boldyreva, E. V (2014). *Cryst. Growth Des.* **14**, 513–522.

Moreno-Calvo, E., Muntó, M., Wurst, K., Ventosa, N., Masciocchi, N. & Veciana, J. (2011). *Mol. Pharm.* **8**, 395–404.

Nowak, M., Dyba, A. J., Janczak, J., Morritt, A., Fábián, L., Karolewicz, B., Khimyak, Y. Z., Braun, D. E. & Nartowski, K. P. (2022). *Mol. Pharm.* **19**, 456–471.

Rigaku Oxford Diffraction (2021).

Shah, H. S., Chaturvedi, K., Hamad, M., Bates, S., Hussain, A. & Morris, K. (2019). *AAPS*

26

PharmSciTech. **20**, 39–49.

Sheldrick, G. M. (1996). *Univ. Gottingen, Inst. Fur Anorg. Chemieder Univ. Tammanstrasse*. **4**, 1999–2003.

Sheldrick, G. M. (2015*a*). *Acta Crystallogr. Sect. C Struct. Chem.* **71**, 3–8.

Sheldrick, G. M. (2015*b*). *Acta Crystallogr. Sect. A Found. Crystallogr.* **71**, 3–8.

Triggle, A. M., Shefter, E. & Triggle, D. J. (1980). *J. Med. Chem.* **23**, 1442–1445.

Ward, M. R. & Oswald, I. D. H. (2020). *Crystals*. **10**, 1–13.

Wu, Y., Kobayashi, A., Halder, G. J., Peterson, V. K., Chapman, K. W., Lock, N., Southon, P. D. & Kepert, C. J. (2008). *Angew. Chemie Int. Ed.* **47**, 8929–8932.

Yang, P., Qin, C., Du, S., Jia, L., Qin, Y., Gong, J. & Wu, S. (2019). *Crystals*. **9**, 367–381.

Zhou, L., Yin, Q., Du, S., Hao, H., Li, Y., Liu, M. & Hou, B. (2016). *RSC Adv.* **6**, 51037–51045.

27

Supporting information

Table S1 Unit cell parameters of six identified polymorphs of NIF.

Form	α (Form A) 100 K(Gui *et al.*, 2020)	β (Form C) 100 K	β' 338 K(Gui *et al.*, 2020)	γ 100 K(Gui *et al.*, 2020)	γ' 250 K(Gui *et al.*, 2020)	δ 100 K(Gui *et al.*, 2020)
Refcode[a]	BICCIZ07	BICCIZ02	BICCIZ08	BICCIZ09	BICCIZ11	BICCIZ12
a (Å)	10.567(3)	9.6661(6)	9.696(2)	19.065(6)	11.435(4)	11.905(4)
b (Å)	10.408(3)	13.7006(8)	14.231(3)	11.506(4)	12.244(4)	10.908(3)
c (Å)	14.788(4)	14.1184(9)	14.463(3)	15.109(5)	12.327(4)	12.779(4)
α (°)	90	61.028(3)	61.90(3)	90	75.535(16)	90
β (°)	95.028(12)	79.631(4)	80.40(1)	108.962(18)	89.055(16)	106.980(9)
γ (°)	90	81.904(4)	81.80(1)	90	84.774(19)	90
Volume (Å^3)	1620.2(8)	1605.89(17)	1731.050	3134.7(18)	1664.2(10)	1587.2(8)
Space Group	$P2_1/c$	$P1$	$P1$	$P2_1/c$	$P1$	$P2_1/n$

[a]   Taken from the CSD. (Groom *et al.*, 2016)

Table S2 Solvents used in the solvent screen study of NIF.

Solvent	Grade	Supplier
Acetonitrile	≥99.9%	Fisher
Butyl acetate	≥99.5%	Sigma Aldrich
1,3-dioxane	98.0%	Alfa Aesar
1,4-dioxane	≥99.0%	Alfa Aesar
Dimethylacetamide	≥99.5%	Sigma Aldrich
Dimethylformamide (anhydrous)	99.8%	Sigma Aldrich
Dimethyl sulfoxide	≥99.9%	Sigma Aldrich
Ethanol	99.8%	Fisher
Ethyl Acetate	≥ 99.7%	Sigma Aldrich

28

Heptane	99.0%	Honeywell
Hexane	≥97.0%	Sigma Aldrich
2-methyltetrahydrofuran	99.0%	Alfa Aesar
Methanol	HPLC	VWR
Morpholine	99.0%	Alfa Aesar
Nitromethane	For synthesis	Merck
2-propanol	ACS Reagent	VWR
Pyridine	≥ 99.0%	Honeywell
Tetrahydrofuran	HPLC ≥ 99.9 %	Honeywell

29

Table S3   Crystallographic data tables of NIF solvates.

	NIF_14DIO	NIF_MORPH	NIF_THF	NIF_PYRI
Chemical formula	$C_{17}H_{18}N_2O_6 \cdot C_2H_4O$	$2(C_{17}H_{18}N_2O_6) \cdot C_4H_9NO$	$2(C_{17}H_{18}N_2O_6) \cdot C_4H_8O$	$C_{17}H_{18}N_2O_6 \cdot C_5H_5N$
M_r	390.38	779.79	764.77	425.43
Crystal system, space group	Triclinic, $P1$	Triclinic, $P1$	Monoclinic, $P2_1/c$	Monoclinic, $P2_1$
Temperature (K)	100	100	100	100
a, b, c (Å)	7.5604 (1), 11.1362 (1), 11.8563 (1)	7.5423 (6), 11.1513 (9), 11.8923 (9)	13.9233 (14), 9.1421 (9), 14.5374 (15)	9.4363 (10), 14.4247 (14), 15.1387 (15)
α, β, γ (°)	73.606 (1), 73.185 (1), 75.643 (1)	73.997 (2), 73.957 (2), 75.253 (2)	96.280 (4)	96.160 (3)
V (Å^3)	901.54 (2)	906.63 (12)	1839.3 (3)	2048.7 (4)
Z	2	1	2	4
Radiation type	Cu Ka	Mo Ka	Mo Ka	Mo Ka
μ (mm^{-1})	0.93	0.11	0.11	0.10
Crystal size (mm)	0.4 × 0.35 × 0.25	0.28 × 0.26 × 0.09	0.32 × 0.13 × 0.07	0.32 × 0.24 × 0.09
Diffractometer	XtaLAB Synergy, Single source at home/near, HyPix3000	Bruker *APEX*-II CCD	Bruker *APEX*-II CCD	Bruker *APEX*-II CCD
Absorption correction	Multi-scan *CrysAlis PRO* 1.171.41.99a (Rigaku Oxford Diffraction, 2021) Empirical absorption correction using	Multi-scan *SADABS2016*/2 (Bruker,2016/2) was used for absorption correction. wR2(int) was 0.0990 before and 0.0322 after correction. The Ratio of minimum	Multi-scan *SADABS2016*/2 (Bruker,2016/2) was used for absorption correction. wR2(int) was 0.1461 before and 0.0550 after correction. The Ratio	Multi-scan *SADABS2016*/2 (Bruker,2016/2) was used for absorption correction. wR2(int) was 0.0794 before and

30

	spherical harmonics, implemented in SCALE3 ABSPACK scaling algorithm.	to maximum transmission is 0.9760. The l/2 correction factor is Not present.	of minimum to maximum transmission is 0.8622. The l/2 correction factor is Not present.	0.0352 after correction. The Ratio of minimum to maximum transmission is 0.9609. The l/2 correction factor is Not present.
T_{min}, T_{max}	0.114, 1.000	0.728, 0.746	0.643, 0.746	0.717, 0.746
No. of measured, independent and observed [$I > 2\sigma(I)$] reflections	21224, 3552, 3543	28798, 4676, 4393	73490, 5614, 4987	54023, 11054, 10804
R_{int}	0.027	0.020	0.036	0.020
$(\sin\theta/\lambda)_{max}$ (Å^{-1})	0.619	0.685	0.715	0.706
$R[F^2 > 2\sigma(F^2)]$, $wR(F^2)$, S	0.036, 0.095, 1.07	0.035, 0.095, 0.97	0.037, 0.102, 1.03	0.029, 0.079, 1.04
No. of reflections	3552	4676	5614	11054
No. of parameters	257	270	275	567
No. of restraints	0	6	5	1
H-atom treatment	H-atom parameters constrained	H atoms treated by a mixture of independent and constrained refinement	H-atom parameters constrained	H-atom parameters constrained
$\Delta\rho_{max}$, $\Delta\rho_{min}$ (e Å^{-3})	0.29, -0.31	0.43, -0.26	0.45, -0.32	0.30, -0.17

31

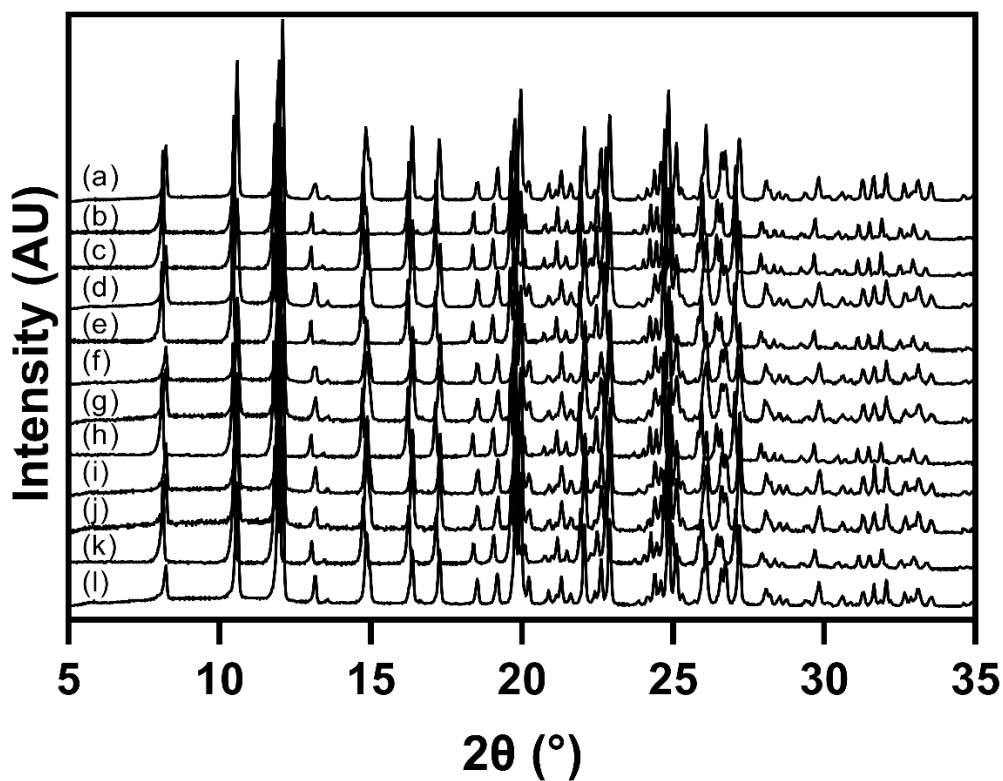|				
Absolute structure	N/A	N/A	N/A	Flack x determined using 4948 quotients [(I+)-(I-)]/[(I+)+(I-)] (Parsons, Flack and Wagner, Acta Cryst. B69 (2013) 249-259).
Absolute structure parameter	N/A	N/A	N/A	0.20 (9)

**Table S4   Contd.** Crystallographic data tables of NIF solvates.

	NIF_DMSO	NIF_DMA	NIF_DMF	NIF_MeOH
Chemical formula	C2H6OS·C17H18N2O6	C17H18N2O6·C4H9NO	C17H18N2O6·C3H7NO	C17H18N2O6·CH4O
Chemical formula	424.46	433.45	419.43	378.37
Crystal system, space group	Triclinic, $P1$	Triclinic, $P1$	Triclinic, $P1$	Monoclinic, P21/c
Temperature (K)	100	173	100	100
a, b, c (Å)	7.9036 (10), 11.8798 (15), 11.9713 (15)	7.6638 (10), 11.6006 (16), 13.9001 (19)	7.4526 (13), 11.647 (2), 13.559 (2)	15.6780 (15), 14.4816 (14), 8.0842 (8)
α, β, γ (°)	67.099 (3), 78.341 (3), 79.126 (4)	65.688 (3), 76.979 (3), 92.932 (3)	70.741 (5), 97.785 (5), 73.470 (5)	104.112 (4)
V (Å^3)	1006.5 (2)	1082.7 (3)	1030.4 (3)	1780.1 (3)
Z	2	2	2	4
Radiation type	Mo Ka	Mo Ka	Mo Ka	Mo Ka
μ (mm^{-1})	0.21	0.10	0.10	0.11
Crystal size (mm)	0.16 × 0.05 × 0.01	0.4 × 0.25 × 0.11	0.34 × 0.15 × 0.08	0.40 × 0.23 × 0.08
Diffractometer	Bruker APEX-II CCD	Bruker APEX-II CCD	Bruker APEX-II CCD	Bruker APEX-II CCD
Absorption correction	Multi-scan SADABS2016/2 (Bruker,2016/2) was used for absorption correction. wR2(int) was 0.1110 before and 0.0630 after	Multi-scan SADABS2016/2 (Bruker,2016/2) was used for absorption correction. wR2(int) was 0.1470 before and 0.0676 after	Multi-scan SADABS2016/2 (Bruker,2016/2) was used for absorption correction. wR2(int) was 0.1093 before and 0.0513 after	Multi-scan SADABS2016/2 (Bruker,2016/2) was used for absorption correction. wR2(int) was

33

|				
	correction. The Ratio of minimum to maximum transmission is 0.7017. The l/2 correction factor is Not present.	correction. The Ratio of minimum to maximum transmission is 0.8046. The l/2 correction factor is Not present.	correction. The Ratio of minimum to maximum transmission is 0.9140. The l/2 correction factor is Not present.	0.1274 before and 0.0492 after correction. The Ratio of minimum to maximum transmission is 0.9302. The l/2 correction factor is Not present.
T_{min}, T_{max}	0.524, 0.746	0.600, 0.746	0.682, 0.746	0.694, 0.746
No. of measured, independent and observed [$I > 2\sigma(I)$] reflections	13422, 5156, 3963	36418, 6605, 5213	35697, 5888, 5050	101200, 5484, 5006
R_{int}	0.054	0.043	0.038	0.032
$(\sin \theta/\lambda)_{max}$ (Å^{-1})	0.705	0.715	0.718	0.717
$R[F^2 > 2\sigma(F^2)]$, $wR(F^2)$, S	0.045, 0.110, 1.02	0.045, 0.130, 1.04	0.037, 0.098, 1.03	0.037, 0.105, 1.03
No. of reflections	5156	6605	5888	5484
No. of parameters	269	309	278	254
No. of restraints	0	13	0	0
H-atom treatment	H-atom parameters constrained	H-atom parameters constrained	H-atom parameters constrained	H atoms treated by a mixture of independent and constrained refinement
$\Delta\rho_{max}$, $\Delta\rho_{min}$ (e Å^{-3})	0.38, −0.56	0.31, −0.23	0.40, −0.27	0.46, -0.39

34

Figure S1 X-ray diffraction pattern of solid material from slurring experiments using: (a) acetonitrile, (b) butyl acetate, (c) 1,3-dioxane, (d) ethanol, (e) ethyl acetate, (f) heptane, (g) hexane, (h) 2-methyltetrahydrofuran, (i) nitromethane, (j) 2-propanol, (k) water and (l) α-NIF as supplied from AlfaAesar.
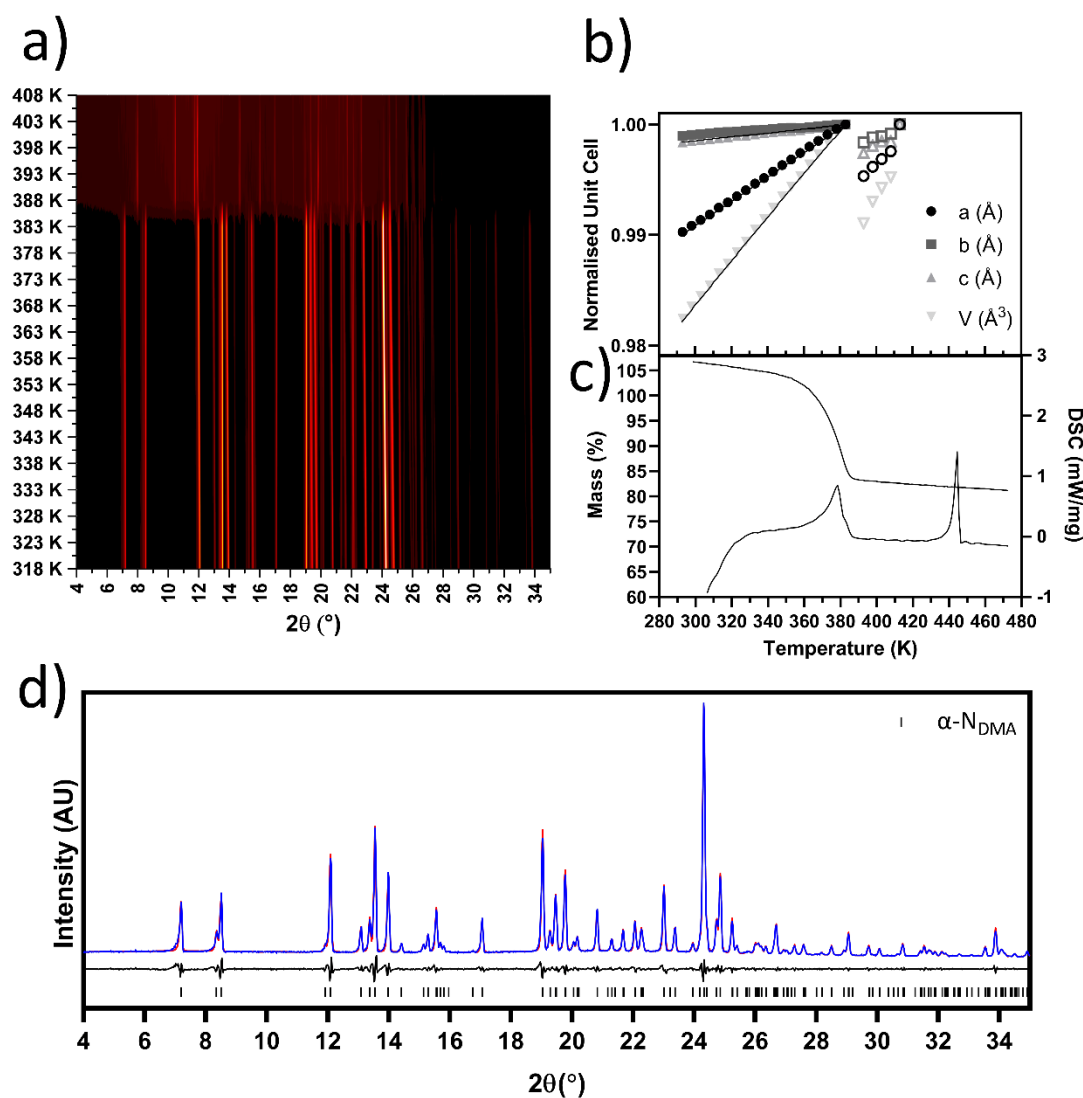
35
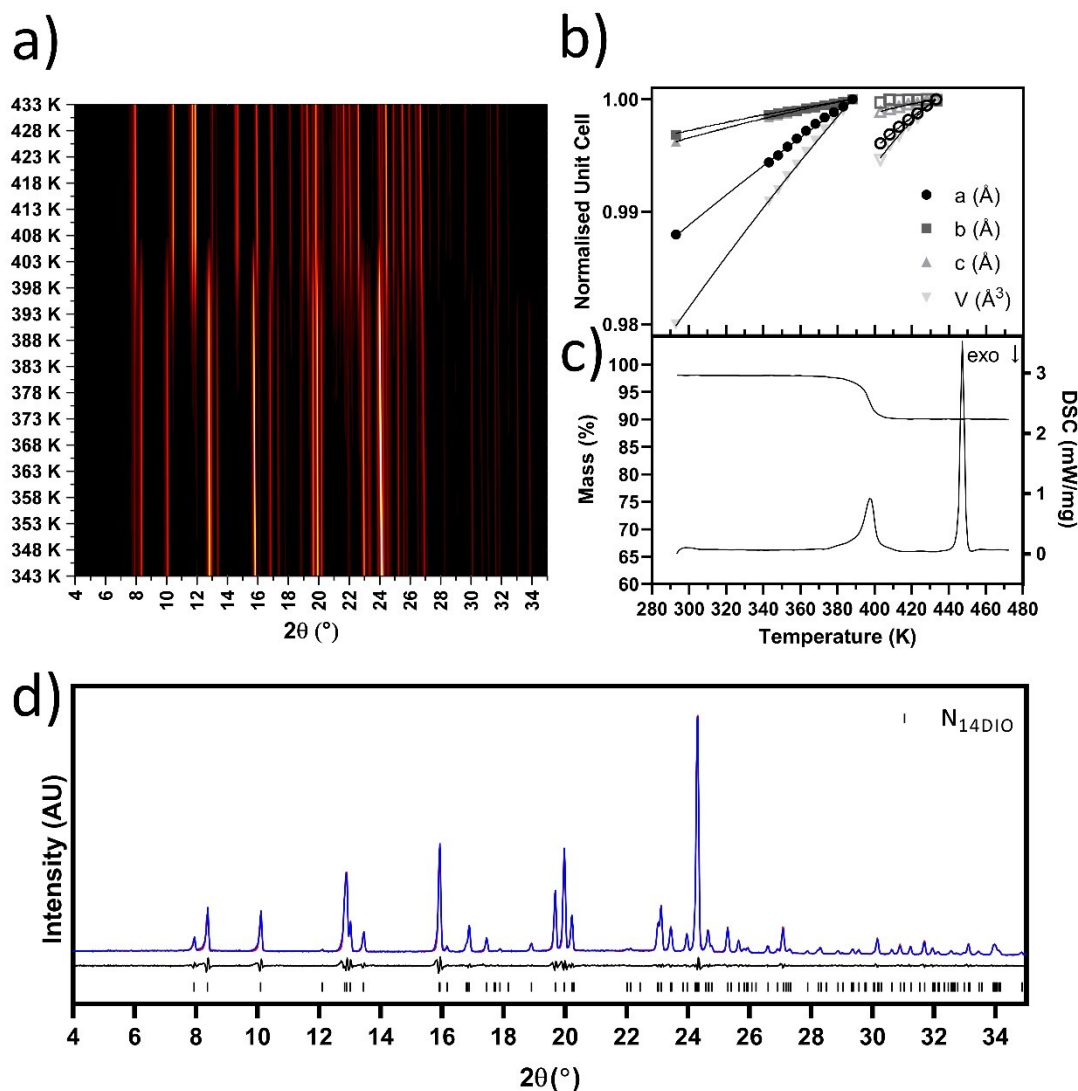
Figure S2 Thermal data of N_{14DIO} capturing the desolvation to the α-form of NIF a) Surface plot of VT-XRPD data from 343 K to 433 K. b) Unit cell parameters from Rietveld refinements of each XRPD pattern. Closed symbols represent data for the solvate, open symbols represent data for desolvated structure. c) DSC and TGA trace for N_{14DIO}. d) XRPD pattern for the 1,4-dioxane solvate collected at 293 K. The experimental data is shown in blue, whilst the calculated profile is shown in red. The difference profile is displayed underneath the diffraction pattern showing that they are in agreement. The calculated reflections are based on the single-crystal data collected for N_{14DIO}.

36
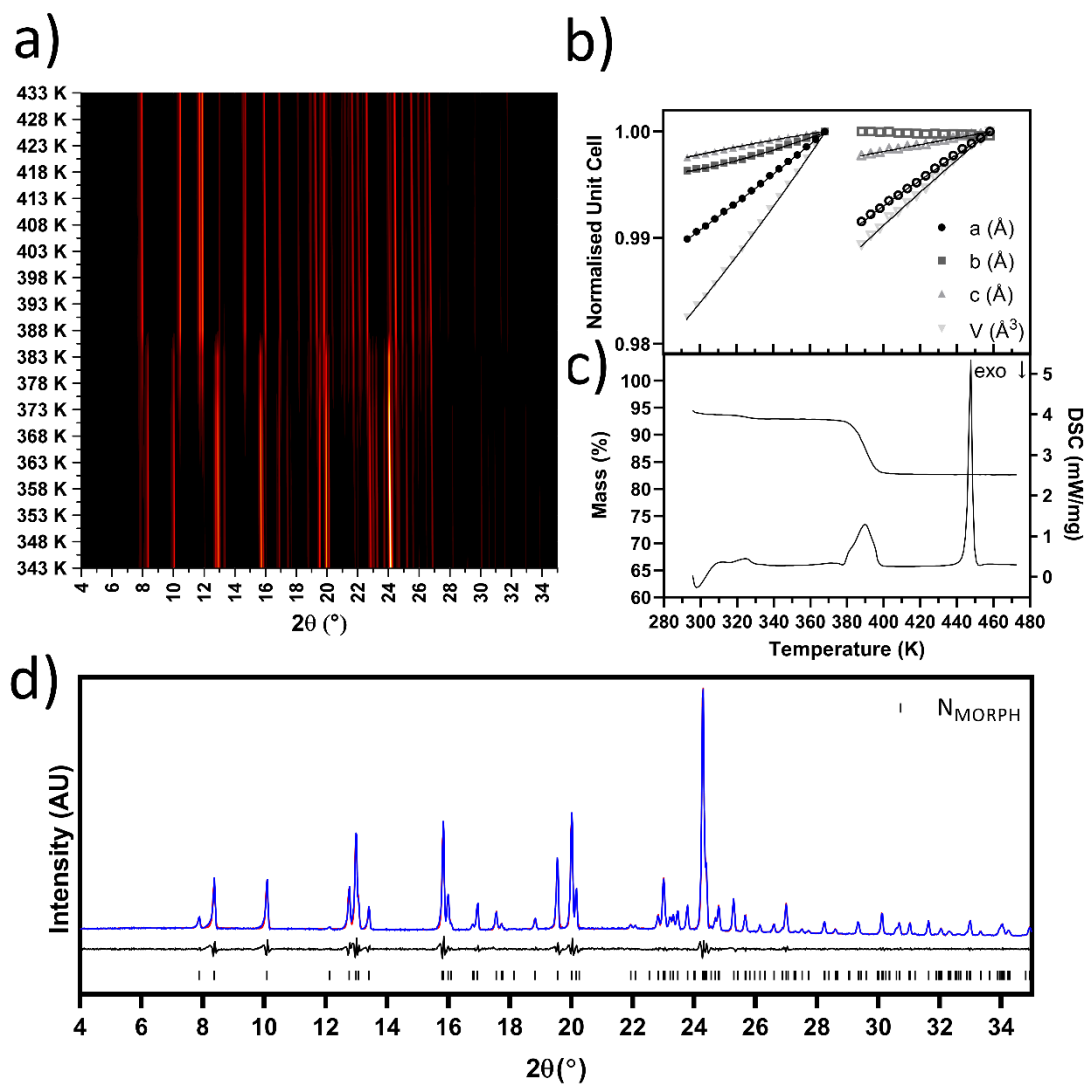
Figure S3 Thermal data of N$_{MORPH}$ capturing the desolvation to the α-form of NIF a) Surface plot of VT-XRPD data from 343 K to 433 K. b) Unit cell parameters from Rietveld refinements of each XRPD pattern. Closed symbols represent data for the solvate; open symbols represent data for desolvated structure. c) DSC and TGA trace for N$_{MORPH}$. d) XRPD pattern for the morpholine solvate collected at 293 K. The experimental data is shown in blue, whilst the calculated profile is shown in red. The difference profile is displayed underneath the diffraction pattern showing that they are in agreement. The calculated reflections are based on the single-crystal data collected for N$_{MORPH}$.

37
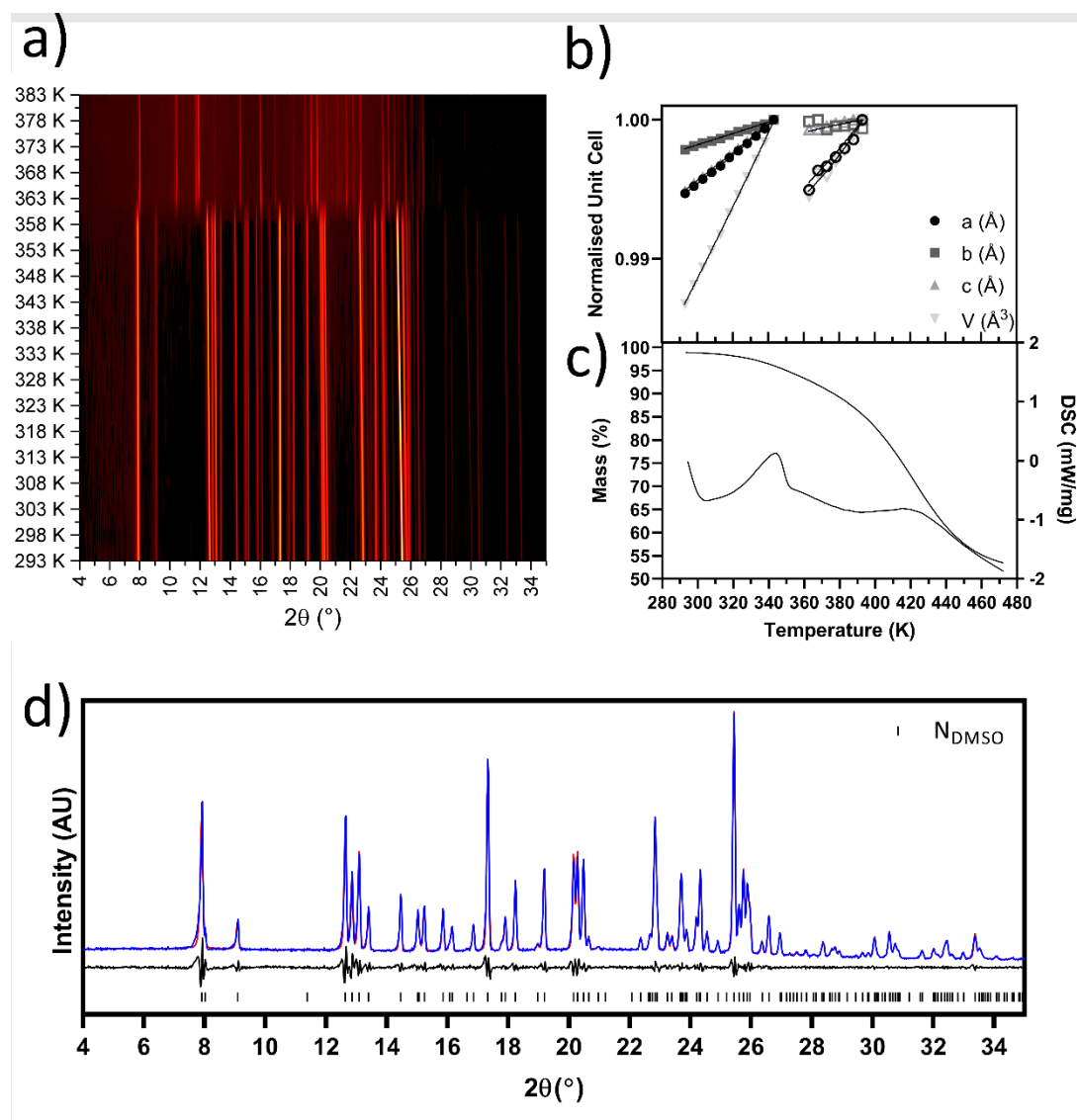
Figure S4 Thermal data of NDMSO capturing the desolvation to α-NIF a) Surface plot of VT-XRPD data from 293 K to 383 K. b) Unit cell parameters from Rietveld refinements of each XRPD pattern. The data could only be fitted to a temperature of 393 K. Closed symbols represent data for the solvate; open symbols represent data for desolvated structure. c) DSC and TGA trace for NDMSO. No prominent melting event is witnessed. d) XRPD pattern for the DMSO solvate collected at 293 K. The experimental data is shown in blue, whilst the calculated profile is shown in red. The difference profile is displayed underneath the diffraction pattern. The calculated reflections are based on the single-crystal data collected for NDMSO.

38

Figure S5 Thermal data of α-N$_{DMA}$ capturing the desolvation to α-NIF a) Surface plot of VT-XRPD data from 293 K to 403 K. Melt of the sample is captured from 388 K. b) Unit cell parameters from Rietveld refinements of each XRPD pattern. The data could only be fitted to a temperature of 413 K. Closed symbols represent data for α-N$_{DMA}$; open symbols represent data for β-N$_{DMA}$ structure. c) DSC and TGA trace for N$_{DMA}$. d) XRPD pattern for the DMA solvate collected at 293 K. The experimental data is shown in blue, whilst the calculated profile is shown in red. The difference profile is displayed underneath the diffraction pattern. The calculated reflections are based on the single-crystal data collected for α-N$_{DMA}$.
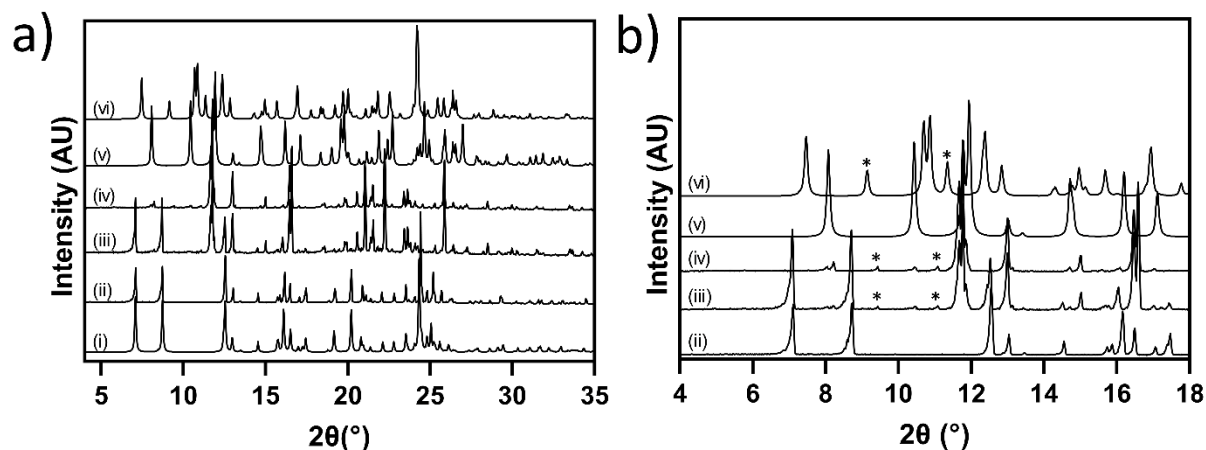
Figure S6 a) XRPD of NDMF solvate from 4 to 35°, 2θ. (i) Simulated powder pattern from SC-data. VT patterns at (ii) 293 K; (iii) 353 K and (iv) 358 K. The latter temperatures show the start of desolvation to α-NIF. (v) Simulated powder pattern of α-NIF from SC-data collected at 297 K and (vi) Powder pattern of β-NIF collected at 296 K (BICCIZ03). b) Expanded view of Figure a, highlighting the region where a form other than α-NIF appears during desolvation and 353 and 358K. Asterisks indicate reflections that might correspond to Form β-NIF but that are significantly shifted in 2-theta.
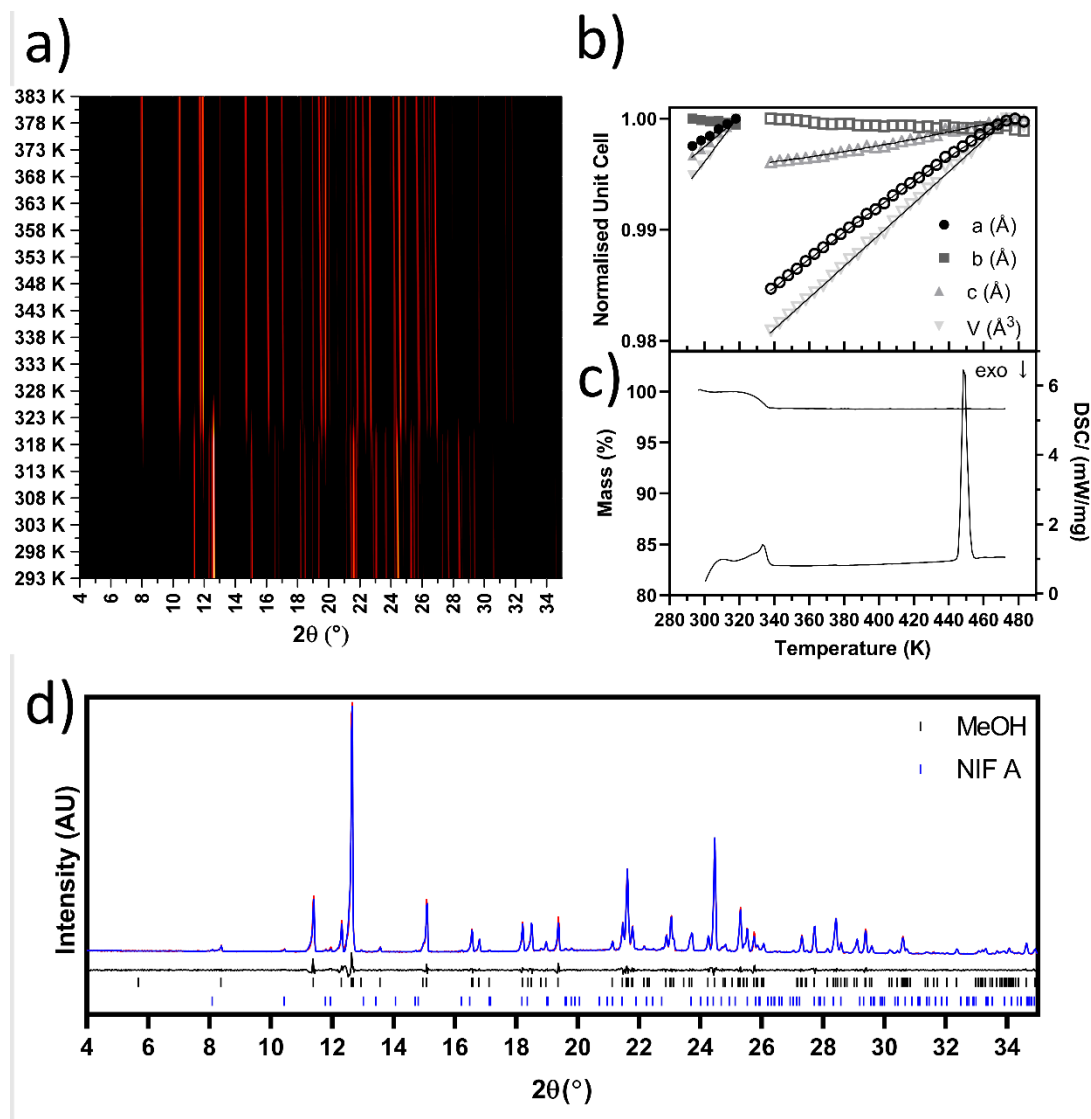
40
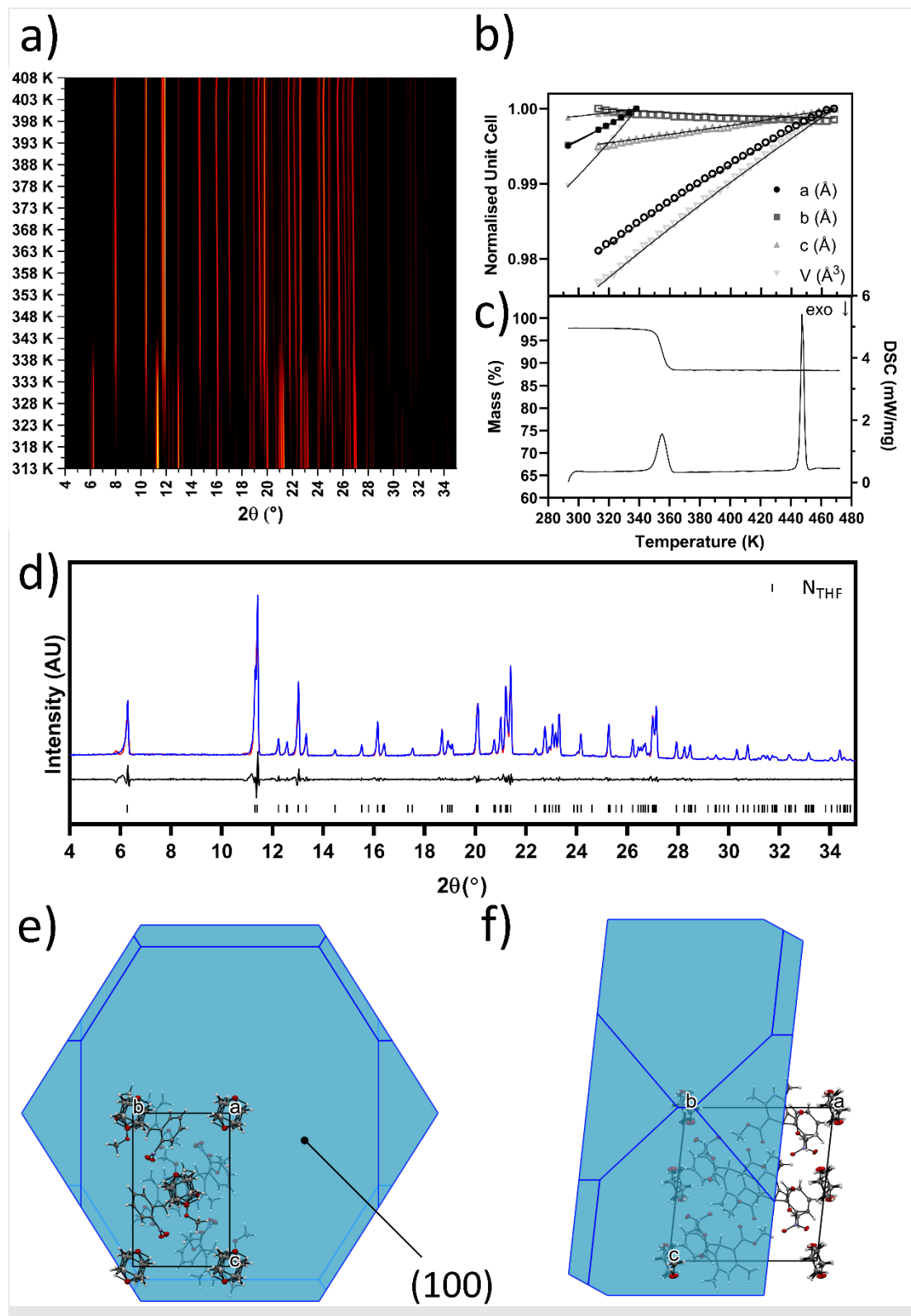
Figure S7 Thermal data of N_{THF} capturing the desolvation to the α-form of NIF a) Surface plot of VT-XRPD data from 313 K to 408 K. b) Unit cell parameters from Rietveld refinements of each XRPD pattern. Closed symbols represent data for the solvate; open symbols represent data for desolvated structure. c) DSC and TGA trace for N_{THF}. d) XRPD pattern for the THF solvate collected

at 293 K. The experimental data is shown in blue, whilst the calculated profile is shown in red. The difference profile is displayed underneath the diffraction pattern showing that they are in agreement. The calculated reflections are based on the single-crystal data collected for N_{THF}. The BFDH morphology for NTHF along e) a-axis and f) b-axis indicating the placement of the THF molecules with respect to the largest face of the crystal. The location of the THF molecules facilitates the loss on heating.
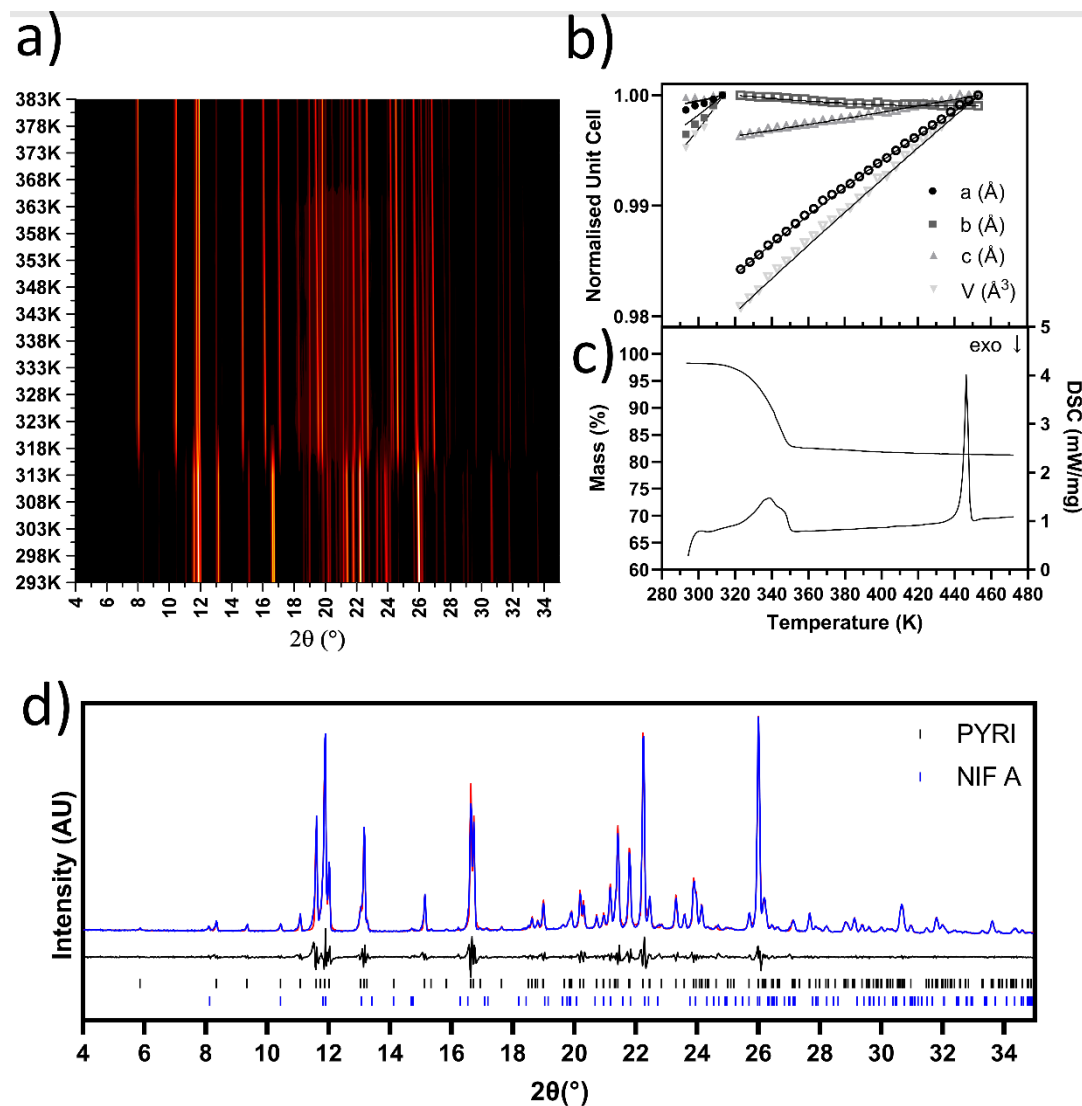
Figure S8 Thermal data of N_{PYRI} capturing the desolvation to the α-form of NIF a) Surface plot of VT-XRPD data from 293 K to 383 K. b) Unit cell parameters from Pawley refinements of each XRPD pattern. Closed symbols represent data for the solvate; open symbols represent data for desolvated structure. c) DSC and TGA trace for N_{PYRI}. d) XRPD pattern for the pyridine solvate collected at 293 K. The experimental data is shown in blue, whilst the calculated profile is shown in red. The difference profile is displayed underneath the diffraction pattern. The calculated reflections are based on the single-crystal data collected for N_{PYRI} and NIF α-form.

42

Figure S9 Thermal data of N_{MeOH} capturing the desolvation to α-NIF a) Surface plot of VT-XRPD data from 293 K to 383 K. b) Unit cell parameters from Pawley refinements of each XRPD pattern. Closed symbols represent data for the solvate; open symbols represent data for desolvated structure. c) DSC and TGA trace for N_{MeOH}. d) XRPD pattern for the DMF solvate collected at 293 K. The experimental data is shown in blue, whilst the calculated profile is shown in red. The difference profile is displayed underneath the diffraction pattern. The calculated reflections are based on the single-crystal data collected for N_{MeOH}. The solvate is only formed from slow evaporation hence the single-crystals were ground for both VT-XRPD and STA. The pulverisation of single-crystals may have induced mechanical desolvation as there was α-NIF present in all of the diffraction patterns as small trace quantities.
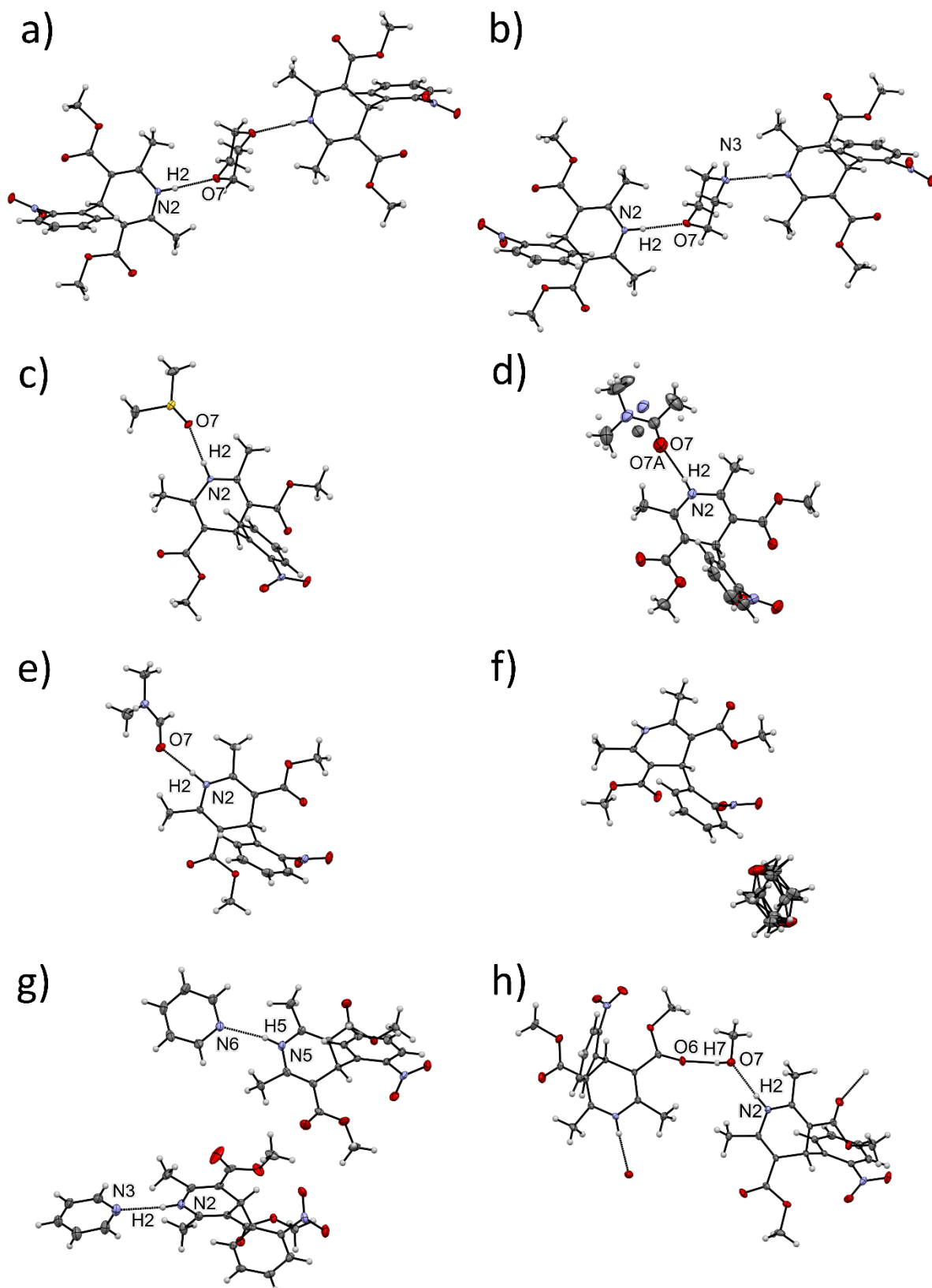
Figure S10 Interactions between NIF and solvents: a) 1,4-dioxane; b) morpholine; c) DMSO; d) DMA (which shows disorder); e) DMF; f) THF (note hydrogen bonding is absent between solvent and

NIF molecule); g) pyridine and h) methanol. Labelled atoms show those which are involved in hydrogen bonds.